Mixed dark matter models for the peculiar compact object in remnant HESS J1731 − 347 and their implications for gravitational wave properties

Bin Hong and ZhongZhou Ren*

School of Physics Science and Engineering, Tongji University, Shanghai 200092, China
and Key Laboratory of Advanced Micro-Structure Materials, Ministry of Education, Shanghai, 200092, China

(Received 10 October 2023; revised 5 December 2023; accepted 8 December 2023; published 2 January 2024)

A recent assessment of the central compact object in the supernova remnant HESS J1731 − 347 [Nat. Astron. **6**, 1444 (2022)] reveals its remarkably small radius, accompanied by the intriguing characteristic of a mass smaller than one solar mass, a feature that has hitherto defied a conclusive explanation. To explain the astrophysical features of this peculiar source, in the present work, we consider two distinct dark matter models: the single-fluid dark matter model and the two-fluid dark matter model, both mixed within neutron stars. These two models can meet various astronomical observational constraints well and successfully account for the observational requirements of HESS J1731 − 347. We further estimate the parameter space of these two dark matter classes in light of multimessenger observational constraints. Additionally, we investigate the effects of these dark matter models on tidal deformability, neutron star nonradial oscillation frequencies, and gravitational waves during the binary neutron star inspiral process. Our findings underscore the pivotal role played by dark matter in shaping the gravitational wave-related properties of neutron stars, thereby offering valuable insights for future observations.

DOI: 10.1103/PhysRevD.109.023002

I. INTRODUCTION

Neutron stars (NSs), as a class of compact objects in the Universe, represent an exceptional platform for scrutinizing the four fundamental interactions of nature [1]. It is widely held that the NS interiors may encompass not only baryon matter but also components such as kaon condensates, quark matter, and even dark matter (DM). The task of discerning these components and providing an accurate description of their equation of states (EOS) has become an imminent scientific conundrum [2,3]. Simultaneously, recent multimessenger observations continually push the boundaries of our understanding of NSs. Notably, discoveries such as NSs with twice the solar mass ($M_\odot$) [4–9], the extraction of tidal deformability in the binary NS merger event GW170817 by the LIGO/Virgo Collaboration [10,11], and the precise measurements of mass and radius for PSR J0030 + 0451 [12,13] and PSR J0740 + 6620 [8,9] by NICER have presented formidable challenges to our understanding of the dense matter composition and structural characteristics within NSs. In response to these challenges, various theoretical frameworks have been proposed, such as the introduction of hyperonic degrees of freedom by adjusting potential well depths to effectively replicate the massive NS observations [14], the development of the BigApple parameters within covariant density functional theory to describe massive NS at the nucleonic level [15], the incorporation of quark matter to account for the GW190814 event [16], and the introduction of isovector-scalar and isoscalar-scalar mesons to successfully explain constraints arising from GW170817 and massive NS observations, as well as heavy-ion collision and PREX-II experiments [17].

However, recently, through the x-ray spectrum and distance estimation obtained from Gaia observations, inferences regarding the radius and mass of the central compact object within the supernova remnant HESS J1731 − 347 have been reported. It is noted that this object exhibits an extraordinarily low mass of $M = 0.77^{+0.20}_{-0.17} M_\odot$ and a compact radius of $R = 10.4^{+0.86}_{-0.78}$ km [18]. This observation suggests that the central compact object within HESS J1731 − 347 could potentially be the lightest known NS to date, characterized by a radius even smaller than the currently known most reliable NS sizes. Such a finding raises concerns about reconciling such a compact object in conventional NS theoretical models. Traditional baryon models, such as the relativistic mean-field (RMF) BigApple parametrized model [15], the density-dependent RMF model [19], and the hyperon RMF model [14], can show more obvious advantages in characterizing massive NSs. However, these models face difficulties in providing a radius smaller than 10 km for low-mass NSs of around $1M_\odot$. Meanwhile, when the mass is below the $1M_\odot$ scale, its formation is considered unsupported by standard stellar

*zren@tongji.edu.cn

evolution [20]. To explain such an unusual object, adjusting or expanding current models to accommodate these unique observational findings may be the best course of action [21–25]. For example, introducing delta mesons in nucleon interactions [25], adopting a quark-core hybrid model [21], or assuming a smaller symmetry energy slope in the baryon model [23] could reconcile the characteristics of HESS J1731 − 347 to some extent. Additionally, a more general hypothesis is that it could be a quark star composed of strange quark matter [24].

It is noteworthy that in compact objects like NSs the interior not only involves interactions between microscopic nuclei, but its strong gravitation also makes it possible to couple DM. Several studies have shown that the presence of DM components has a significant effect on NS mass-radius relationship [26–28] and thus are expected to yield lower mass and smaller radius. In the ΛCDM cosmic model, DM constitutes 24% of total energy in the Universe, and its existence has been predicted by various observations, including galaxy rotation curves, the cosmic microwave background, and gravitational lensing [29,30]. Recently, the James Webb Space Telescope's measurements of some young galaxies [31], accompanied by the indirect detection of infrared spectra from the DM decay [32] or DM capture in old NSs [33], might bring about new questions about the DM component and its interaction in the Universe. Meanwhile, there is still a lack of precise description of DM, with research primarily focused on the search and validation of candidate particles, such as PandaX-II [34], which holds promise in detecting potential Fermi dark matter signals. Although DM typically does not directly interact with ordinary matter, it exerts significant gravitational effects on compact bodies [35]. When DM extended to NS studies, it can affect various observational properties [26–28]. In turn, NSs also serve as an excellent observational platforms for assessing DM capture rates [36] and constraining DM models [37].

In light of the NS's important role as a gravitational wave source, especially the merger of binary NSs can generate powerful gravitational wave signals, which yields significant implications for understanding binary star dynamics, electromagnetic radiation processes, and the origin of heavy elements [38,39]. Additionally, NS nonradial oscillation, as another important source of gravitational waves, also carries extensive information about the NS interior [40]. With the advent of new observational instruments like the Einstein Telescope and Cosmic Explorer [41–43], there is potential to gain deeper insight into gravitational wave observations from NS-related processes, making theoretical research in this area increasingly urgent.

In this study, we introduce two classes of DM-mixed NS models within the RMF framework to explain the observational outcomes of HESS J1731 − 347. Furthermore, we also analyze the differences in NS-related gravitational wave properties between these two DM models and explore their impacts on the tidal deformability and nonradial oscillation frequencies as well as the gravitational wave emissions during the binary NS inspiral process. The following is the organization of this paper. In Sec. II, we provide an introduction to the construction of baryon components as well as two types of DM components; we also examine the possible distribution of DM within NSs and further constrain the DM parameter space by incorporating observational data. In Sec. III, we discuss the role of DM in tidal deformability, oscillation frequencies, and binary NS inspiral gravitational wave. Section IV provides a brief summary of the entire research work.

II. BARYON MATTER AND TWO DARK MATTER MODELS

A. Baryon matter model

The relativistic mean-field theory, as a phenomenological many-body theory [44–46], exhibits unique advantages in describing finite nuclei and infinite nuclear matter. In the RMF framework, the interaction among baryons occurs through the exchange of mesons [44–46]. To describe the nature of nuclear forces, RMF models commonly encompass four types of mesons. The scalar-isoscalar meson σ is utilized to characterize medium-range attraction in nuclear forces, the vector-isoscalar meson ω is employed to characterize short-range repulsion, while the vector-isovector meson ρ and the scalar-isovector meson δ are dedicated to depicting the isospin properties among nucleons and exhibit a capacity to effectively characterize the symmetry energy and its slope in nuclear matter. In this study, we adopt the simplest version within the RMF theory, namely, the "$\sigma\omega\rho$" three-meson exchange model, as it has extensive application in investigating the properties of nuclear matter and NSs [47–53]. The Lagrangian density of this model can typically be expressed as a sum of $L = L_N + L_l + L_\sigma + L_\omega + L_\rho + L_{\rho-\omega}$, where $L_N, L_l, L_\sigma, L_\omega, L_\rho, L_{\rho-\omega}$ represent the Lagrangian of the nucleon, lepton, three mesons (σ, ω, ρ), and $\rho - \omega$ coupling term, respectively, and they can be written as [44–46]

$$L_N = \sum_{N=n,p} \bar{\psi_N}\Big(i\partial_\mu\gamma^\mu - m_N + g_\sigma\sigma - g_\omega\omega_\mu\gamma^\mu - \frac{1}{2}g_\rho\vec{\rho}_\mu\gamma^\mu\vec{\tau}\Big)\psi_N, \tag{1}$$

$$L_l = \sum_{l=e,\nu} \bar{\psi}_l\,(i\partial_\mu\gamma^\mu - m_l)\psi_l, \tag{2}$$

$$L_\sigma = \frac{1}{2}\partial_\mu\sigma\partial^\mu\sigma - \frac{1}{2}m_\sigma^2\sigma^2 - \frac{1}{3}bm_N(g_\sigma\sigma)^3 - \frac{1}{4}c(g_\sigma\sigma)^4, \tag{3}$$

$$L_\omega = -\frac{1}{4}(\partial_\mu\omega_v - \partial_v\omega_\mu)(\partial^\mu\omega^\nu - \partial^\nu\omega^\mu) + \frac{1}{2}m_\omega^2\omega_\mu\omega^\mu, \tag{4}$$

$$L_\rho = -\frac{1}{4}(\partial_\mu\vec{\rho}_v - \partial_\nu\vec{\rho}_\mu)(\partial^\mu\vec{\rho}^\nu - \partial^\nu\vec{\rho}^\mu) + \frac{1}{2}m_\rho^2\vec{\rho}_\mu\vec{\rho}^\mu, \quad (5)$$

$$L_{\rho-\omega} = \Lambda_\omega(g_\rho^2\rho^\mu\rho_\mu)(g_\omega^2\omega^\mu\omega_\mu). \quad (6)$$

where N and l, respectively, represent nucleons (n,p) and leptons (e,μ) in the NS beta-equilibrium system and m_i (where $i = N, \sigma, \omega, \rho$) represents the nucleon and various meson masses.

The Lagrangian densities above, when substituted into the Euler-Lagrange equation, yield respective motion equations. Numerical solutions of these nonlinear equations pose considerable challenges. In the RMF theory, considering the Fermi energy of baryon matter inside a NS is sufficiently high due to its high density, far exceeding its thermal motion, the NS can be treated as zero-temperature system. At this point, within the mean-field approximation, the field operators are approximated by their ground-state expectation values, i.e., $\bar{\psi}\psi \Rightarrow \langle\bar{\psi}\psi\rangle$, $\bar{\psi}\gamma^\mu\psi \Rightarrow \langle\bar{\psi}\gamma^0\psi\rangle = \langle\psi^+\psi\rangle$, $\hat{\sigma} \Rightarrow \sigma_0$, $\hat{\omega} \Rightarrow \omega_0$, $\hat{\rho} \Rightarrow \rho_0$. Consequently, the motion equations corresponding to the Lagrangian are simplified to

$$\left(i\partial_\mu\gamma^\mu - m_N + g_\sigma\sigma_0 - g_\omega\omega_0\gamma^0 - \frac{1}{2}g_\rho\rho_0\gamma^0\tau_3\right)\psi_N = 0, \quad (7)$$

$$(i\partial_\mu\gamma^\mu - m_l)\psi_l = 0, \quad (8)$$

$$g_\sigma\sigma_0 = \left(\frac{g_\sigma}{m_\sigma}\right)^2[\langle\bar{\psi}\psi\rangle_p + \langle\bar{\psi}\psi\rangle_n - g_2\sigma_0^2 - g_3\sigma_0^3], \quad (9)$$

$$g_\omega\omega_0 = \left(\frac{g_\omega}{m_\omega}\right)^2[\langle\psi^+\psi\rangle_p + \langle\psi^+\psi\rangle_n - 2\Lambda_\omega(g_\rho\rho_0)^2(g_\omega\omega_0)], \quad (10)$$

$$g_\rho\rho_0 = \left(\frac{g_\rho}{m_\rho}\right)^2\left[\frac{\langle\psi^+\psi\rangle_p - \langle\psi^+\psi\rangle_n}{2} - 2\Lambda_\omega(g_\rho\rho_0)(g_\omega\omega_0)^2\right], \quad (11)$$

where the expectation value $\langle\psi^+\psi\rangle_{N=n,p}$ being nucleon $N(n,p)$ vector density n_N^v, can be expressed in terms of nucleon Fermi momentum k_N as

$$\langle\psi^+\psi\rangle_{N=n,p} = n_N^v = \frac{1}{\pi^2}\int_0^{k_N} k^2 dk = \frac{k_N^3}{3\pi^2}, \quad (12)$$

the expectation value $\langle\bar{\psi}\psi\rangle_{N=n,p}$ is nucleon scalar density n_N^s, which depends on the Fermi momentum k_N and the effective mass m_N^* expressed in the form $m_N^* = m_N - g_\sigma\sigma_0$, can be written as

$$\langle\bar{\psi}\psi\rangle_{N=n,p} = n_N^s = \frac{1}{\pi^2}\int_0^{k_N}\frac{k^2 m_N^*}{\sqrt{k^2 + m_N^{*2}}}dk. \quad (13)$$

Based on the energy-momentum tensor

$$\mathcal{T}^{\mu\nu} = \frac{\partial\mathcal{L}}{\partial(\partial_\mu\psi)}\partial^\nu\psi - g^{\mu\nu}\mathcal{L}, \quad (14)$$

the energy density and pressure of baryon matter (BM) can be expressed as

$$\begin{aligned}\varepsilon_{\rm BM} = \mathcal{T}^{00} &= \sum_N\langle\psi_N^+ i\dot{\psi}_N\rangle + \sum_l\langle\psi_l^+ i\dot{\psi}_l\rangle + \frac{1}{2}m_\sigma^2\sigma_0^2 \\ &- \frac{1}{2}m_\omega^2\omega_0^2 - \frac{1}{2}m_\rho^2\rho_0^2 - \Lambda_\omega(g_{\rho N}\rho_0)^2(g_{\omega N}\omega_0)^2 \\ &+ \frac{1}{3}g_2\sigma_0^3 + \frac{1}{4}g_3\sigma_0^4, \end{aligned} \quad (15)$$

$$\begin{aligned}p_{\rm BM} = \frac{1}{3}\mathcal{T}^{ii} &= \frac{1}{3}\sum_N\langle\psi_N^+(-i\alpha\cdot\nabla)\psi_N\rangle \\ &+ \frac{1}{3}\sum_l\langle\psi_l^+(-i\alpha\cdot\nabla)\psi_l\rangle - \frac{1}{2}m_\sigma^2\sigma_0^2 + \frac{1}{2}m_\omega^2\omega_0^2 \\ &+ \frac{1}{2}m_\rho^2\rho_0^2 + \Lambda_\omega(g_{\rho N}\rho_0)^2(g_{\omega N}\omega_0)^2 - \frac{1}{3}g_2\sigma_0^3 - \frac{1}{4}g_3\sigma_0^4, \end{aligned} \quad (16)$$

where the expectation values $\langle\psi_N^+ i\dot{\psi}_N\rangle$ and $\langle\psi_l^+ i\dot{\psi}_l\rangle$ are expressed as

$$\langle\psi_N^+ i\dot{\psi}_N\rangle = g_\omega\omega_0 n_N^v + \frac{1}{\pi^2}\int_0^{k_F} k^2\sqrt{k^2 + (m_N^*)^2}dk, \quad (17)$$

$$\langle\psi_l^+ i\dot{\psi}_l\rangle = \frac{1}{\pi^2}\int_0^{k_F} k^2\sqrt{k^2 + (m_l)^2}dk \quad (18)$$

and the expectation values $\langle\psi_N^+(-i\alpha\cdot\nabla)\psi_N\rangle$ and $\langle\psi_l^+(-i\alpha\cdot\nabla)\psi_l\rangle$ are

$$\langle\psi_N^+(-i\alpha\cdot\nabla)\psi_N\rangle = \frac{1}{\pi^2}\int_0^{k_F}\frac{k^4}{\sqrt{k^2 + (m_N^*)^2}}dk, \quad (19)$$

$$\langle\psi_l^+(-i\alpha\cdot\nabla)\psi_l\rangle = \frac{1}{\pi^2}\int_0^{k_F}\frac{k^4}{\sqrt{k^2 + (m_l^*)^2}}dk. \quad (20)$$

The system involves coupling parameters of $g_{\sigma N}, g_{\omega N}, g_{\rho N}, g_2, g_3, \Lambda_\omega$, which are usually determined by fitting saturation nuclear matter properties like the incompressibility coefficient K, nucleon effective mass m^*, binding energy per nucleon E/A, saturation density n_0, symmetry energy $J_{\rm sym}$, and its slope L. Among these, $J_{\rm sym}$ and L are pivotal in characterizing neutron-rich nuclei, with significant implications for astrophysical phenomena like supernova nucleosynthesis and NS mergers [54], yet their exact values, especially at a supersaturated density, remain uncertain. Despite recent experiments providing a relatively well-determined $J_{\rm sym}$ roughly located at 31.6 ± 2.7 MeV [54–56], significant uncertainties still persist in the value

TABLE I. The parameter set GM1 [62] and its corresponding saturation nuclear properties adopted in this work. The saturation properties include incompressibility coefficient K, nucleon effective mass m^*, binding energy per nucleon E/A, saturation density n_0, symmetry energy $J_{\rm sym}$, and its slope L. In addition to GM1, we also consider other three different sets of relativistic parameters: BigApple [15], FSUGold [68], and IU-FSU [69].

	GM1	BigApple	FSUGold	IU-FSU
m_σ (MeV)	512	492.73	491.5	491.5
m_ω (MeV)	783	782.5	782.5	782.5
m_ϱ (MeV)	770	763	763	763
$n_0(\mathrm{fm}^{-3})$	0.153	0.155	0.1484	0.155
K (MeV)	300	227.001	230.0	231.33
m^*/m	0.70	0.608	0.61	0.61
$-E/A$ (MeV)	16.3	16.344	16.28	16.4
$J_{\rm sym}$ (MeV)	32.5	31.315	32.59	31.3
L (MeV)	94	39.8	60.5	47.21
g_σ	8.910	9.6699	10.5924	9.9712
g_ω	10.610	12.316	14.3019	13.032
g_ϱ	8.196	14.16178	11.767	13.5899
$g_2(\mathrm{fm}^{-1})$	9.7601	11.9173	4.2766	16.75
g_3	−6.3024	−31.6793	49.934	48.76
Λ_ω	0	0.047471	0.03	0.046
ξ	0	0.0007	0.06	0.03

of L [57–59], particularly the significant discrepancies extracted from the very recent experiment PREX-II [60] and CREX [61]. Currently, there are several excellent sets of coupling parameters within the RMF framework that perform remarkably well in describing nuclear physics and NS properties. In the paper, we chose the parameter set GM1 [62] introduced by Glendenning and Moszkowski in the 1990s as our research parameter. This work focus on the possibility that a DM-mixed NS will explain the peculiar compact object in remnant HESS J1731 − 347, while for the baryon model, we just expect it can provide massive NS observations. Although we cannot claim that GM1 is the most ideal parameter model, its form is simple, and associated symmetry energy $J_{\rm sym} = 32.5$ MeV and slope $L = 94$ MeV [62] both fall within the currently acceptable range. Furthermore, GM1 has also been frequently employed within RMF by several recent studies [63–67]. To avoid giving an overly absolute conclusion under GM1, we also considered other three other relativistic parameters BigApple [15], FSUGold [68], and IU-FSU [69], as shown in Table I.

B. Dark matter model

For the DM component, we employ two distinct models. One of these considers the interaction between DM and baryon matter through the exchange of Higgs bosons, and it has recently found extensive application in the study of NSs, such as the investigation of mixed-DM NSs incorporating short-range correlation effects [27] and the examination of the impact of hyperon effects [70] on the mixed-DM NS properties. An advantageous aspect of this model arises when dealing with the hydrostatic equilibrium equations, as the interaction between dark matter and baryon matter, akin to meson exchange interactions among nucleons, allows for the application of a single-fluid Tolman-Oppenheimer-Volkoff (TOV) equation. Consequently, within this model, DM is uniformly distributed within NSs, and for brevity, we refer to this as the single-fluid model hereafter. In this section, we choose the lightest neutralino with the Fermi DM mass of $M_\chi = 200$ GeV as the candidate. Since direct interactions between DM and nucleons are absent, they interact only through coupled Higgs fields, and their Lagrangian form can be described as [71]

$$\begin{aligned}\mathcal{L}_{\rm DM} = \bar{\chi}[i\gamma^\mu\partial_\mu - M_\chi + yh]\chi + \frac{1}{2}\partial_\mu h\partial^\mu h \\ - \frac{1}{2}M_h^2h^2 + \sum_N f\frac{m_N}{v}\bar{\psi}_N h\psi_N,\end{aligned} \tag{21}$$

in which m_N represents the nucleon mass and M_h is Higgs boson with a value of 125 GeV. The variables h and χ signify the Higgs and DM fields; y is the coupling strength between them, typically ranging from 0.001 to 0.1; and we adopt a typical value of 0.07 for this study [71,72]. $f\frac{m_N}{v}$ is the effective Yukawa coupling strength between nucleons and Higgs bosons, where f is the Higgs-nucleon formation factor, typically taken as 0.3, and v is the Higgs vacuum expectation value, which is 246 GeV. Our selection of these values, based on lattice computations, aligns with the DM-nucleon scattering cross section experimental in PandaX-II [34] and PandaX-4T [73]. Additionally, we assume that the density of DM inside NSs is roughly lower than that of nuclear matter by a factor of 1000. For a typical saturation nuclear matter density $n_0 = 0.16\ \mathrm{fm}^{-3}$, the corresponding DM Fermi momentum k_F is approximately 0.033 GeV.

According to the mean-field approximation, the energy density and pressure of DM components are given by

$$\varepsilon_{\rm DM} = \frac{1}{\pi^2}\int_0^{k_F^{\rm DM}} k^2\,\mathrm{d}k\sqrt{k^2 + (M_\chi^\star)^2} + \frac{1}{2}M_h^2h_0^2 \tag{22}$$

and

$$p_{\rm DM} = \frac{1}{3\pi^2}\int_0^{k_F^{\rm DM}} \frac{k^4\mathrm{d}k}{\sqrt{k^2 + (M_\chi^\star)^2}} - \frac{1}{2}M_h^2h_0^2. \tag{23}$$

The nucleon and DM effective masses are donated by $M_N^\star$ and $M_\chi^\star$, and $\rho_s^{\rm DM}$ represents the DM scalar density; they are expressed as follows:

$$M_N^\star = m_N - g_{\sigma N}\sigma_0 - \frac{fm_N}{v}h_0, \tag{24}$$

$$M_\chi^\star = M_\chi - y h_0, \tag{25}$$

$$\rho_s^{\mathrm{DM}} = \frac{M_\chi^*}{\pi^2}\int_0^{k_F^{\mathrm{DM}}} \frac{k^2 \mathrm{d}k}{(k^2 + M_\chi^{*2})^{1/2}}, \tag{26}$$

The energy density and pressure of the entire DM-mixed NS system need to be brought into the TOV equation as inputs, and for the single-fluid model, the static spherically symmetric space-time background used here is

$$ds^2 = -e^{\nu(r)}dt^2 + e^{\lambda(r)}dr^2 + r^2(d\theta^2 + \sin^2\theta d\phi^2), \tag{27}$$

and TOV equations can be derived from the Einstein field equations [74],

$$\begin{aligned} \frac{\mathrm{d}p}{\mathrm{d}r} &= -\frac{(p+\epsilon)(M + 4\pi r^3 p)}{r(r-2M)}, \\ \mathrm{d}M &= 4\pi r^2 \epsilon \mathrm{d}r, \end{aligned} \tag{28}$$

where $\varepsilon = \varepsilon_{\mathrm{BM}} + \varepsilon_{\mathrm{DM}}$ and $p = p_{\mathrm{BM}} + p_{\mathrm{DM}}$, and the metric functions are expressed as

$$\begin{aligned} \mathrm{e}^{\lambda(r)} &= (1 - 2m/r)^{-1}, \\ \nu(r) &= 2\int_r^\infty dr' \frac{\mathrm{e}^{\lambda(r')}}{r'^2}(m + 4\pi r'^3 p). \end{aligned} \tag{29}$$

In the standard NS calculation scheme, for the outer crust of BM component, where the density located approximately around $6.3\times10^{-12}\ \mathrm{fm}^{-3} \leqslant n \leqslant 2.46\times10^{-4}\ \mathrm{fm}^{-3}$, we employ the Baym-Pethick-Sutherland EOS [75]. Moving to the inner crust region, where the density falls within the range of $2.46\times10^{-4}\ \mathrm{fm}^{-3} \leqslant n \leqslant n_t$, we utilize the polytropic parametrized EOS of the form $P = a + b\epsilon^{4/3}$ [76,77], where a and b associated with the core-crust transition density n_t are determined using the thermodynamic method [78–80]. After taking into account the charge neutrality and β-equilibrium conditions, the mass-radius relationship for the DM-mixed NS system will be determined.

Another class of DM models, unlike the single-fluid model where nongravitational interactions between baryon and DM components occur through the exchange of mesons, postulates the existence of solely gravitational interactions between them. Consequently, when solving for a DM-mixed NS, the ideal single-fluid TOV equations are replaced by a two-fluid one (for specific derivations, refer to Refs. [81,82]),

$$\begin{aligned} \frac{\mathrm{d}p_B}{\mathrm{d}r} &= -\frac{(p_B+\epsilon_B)(M + 4\pi r^3 p)}{r(r-2M)}, \\ \frac{\mathrm{d}p_D}{\mathrm{d}r} &= -\frac{(p_D+\epsilon_D)(M + 4\pi r^3 p)}{r(r-2M)}, \\ \mathrm{d}M_B &= 4\pi r^2 \epsilon_B \mathrm{d}r, \qquad \mathrm{d}M_D = 4\pi r^2 \epsilon_D \mathrm{d}r, \end{aligned} \tag{30}$$

where B and D, respectively, represent the BM and DM components, while M denotes the total gravitational mass. The crust of the BM component adopts the same EOS as the single-fluid model. The proportion of DM within the NS is represented as $f_{\mathrm{DM}} = M_D/M$.

In the following discussion, we refer to this model as the two-fluid model and assume the DMs are asymmetric fermionic particles [83], with their self-interactions mediated by the ϕ mediator through a repulsive Yukawa potential,

$$V = \frac{\alpha_\chi}{r}\exp(-m_\phi r), \tag{31}$$

where α_χ represents the fine-structure constant of DM coupling to dark mediator and we fix $\alpha_\chi = 10^{-3}$ in this work, m_ϕ is the mediator mass, and r denotes the distance between particles. To provide a DM self-interaction cross section consistent with numerical simulation results, the mediator mass m_ϕ is typically constrained to be below $50\sim60$ GeV [84,85], although this constraint still carries some uncertainty. Theoretical studies mainly focus around 10 GeV [83,86], and for this reason, we also adopt this constraint in this study, exploring mediator masses within the range of $8\sim16$ GeV in the two-fluid DM model. The energy density of DM can be expressed as

$$\varepsilon_{\mathrm{DM}} = \varepsilon_{\mathrm{kin}} + \varepsilon_{\mathrm{Y}}, \tag{32}$$

in which $\varepsilon_{\mathrm{kin}}$ and ε_{Y} represent the kinetic energy and Yukawa potential energy density. The system pressure is related thermodynamically as

$$p_{\mathrm{DM}} = n\frac{\partial\varepsilon_{\mathrm{DM}}}{\partial n} - \varepsilon_{\mathrm{DM}}, \tag{33}$$

where n represents the Fermi DM number density. Like the baryon matter mentioned above, here we assume that the DM temperature is significantly lower than its Fermi momentum, so DM component can be also treated as zero-temperature system. According to the principles of statistical mechanics, the number density, kinetic energy density, and pressure of DM can be expressed in the forms

$$n = \frac{g_s}{(2\pi)^3}\int_0^{p_F} 4\pi p^2 dp = \frac{g_s m_\chi^3}{6\pi^2}x^3, \tag{34}$$

$$\varepsilon_{\mathrm{kin}} = \frac{g_s}{(2\pi)^3}\int_0^{p_F} E(p) 4\pi p^2 dp = \frac{g_s}{2}m_\chi^4 \xi(x), \tag{35}$$

$$p_{\mathrm{kin}} = \frac{1}{3}\frac{g_s}{(2\pi)^3}\int_0^{p_F}\frac{p^2}{E(p)}4\pi p^2 dp = \frac{g_s}{2}m_\chi^4\psi(x), \tag{36}$$

where $E = \sqrt{p^2 + m_\chi^2}$ represents the relativistic energy dispersion relation and g_s denotes the DM spin. $m_\chi = 2$ GeV is the DM mass, and the $\xi(x)$ and $\psi(x)$ are defined as [87]

$$\xi(x) = \frac{1}{8\pi^2}\{x\sqrt{1+x^2}(1+2x^2) - \ln[x+\sqrt{1+x^2}]\},$$

$$\psi(x) = \frac{1}{8\pi^2}\{x\sqrt{1+x^2}(2x^2/3-1) + \ln[x+\sqrt{1+x^2}]\},$$

in which x is defined as p_F/m_χ. To determine the total Yukawa potential energy, it is theoretically necessary to sum over all DM particles and subsequently approximate the integral over their volume elements as

$$\varepsilon_Y = \frac{2\pi\alpha_\chi n^2}{m_\phi^2} = \frac{\alpha_\chi g_s^2}{18\pi^3}\frac{m_\chi^6}{m_\phi^2}x^6. \quad (37)$$

Thus, the total energy density and pressure of the DM component are [86]

$$\varepsilon_{DM} = \frac{g_s}{2}m_\chi^4\xi(x) + \frac{\alpha_\chi g_s^2}{18\pi^3}\frac{m_\chi^6}{m_\phi^2}x^6, \quad (38)$$

$$p_{DM} = \frac{g_s}{2}m_\chi^4\psi(x) + \frac{\alpha_\chi g_s^2}{18\pi^3}\frac{m_\chi^6}{m_\phi^2}x^6. \quad (39)$$

In the following discussion, we opt to investigate mediator mass m_ϕ and Fermi momentum k_F as variables, as these two parameters profoundly reflect the nature of DM interaction strength and DM mass, and their precise values are still uncertain. Figure 1 illustrates the function of mass as radius under these two different DM models. The upper panel displays the mass-radius relationships in the two-fluid scenario, in which the light green lines represent the mass-radius relationship for DM components under different mediator masses m_ϕ from 8 to 16 MeV, while the purple lines address the mass-radius trend for corresponding BM components. The orange region represents the total gravitational mass-radius relationship, where the mass is the sum of the DM and the BM that is not a simple superposition of respective components; instead, we assume that the central pressure for both DM and BM components has the same initial value and integrate the two-fluid TOV equation to obtain the mass-radius relationships. Since the DM component radius cannot be directly observed, the system radius is usually assumed to be the BM component radius, which is in line with a common convention employed in astrophysical studies. Moreover, as m_ϕ increases, the DM component mass and radius decrease continuously, whereas the mass and radius of BM component just show the opposite trend. Although the maximum mass cannot support $2M_\odot$ when m_ϕ exceeds 16 MeV, the mass-radius relationships provided by this two-fluid model can still be matched well the observational data of HESS J1713 − 347, as shown by the light cyan shaded region. The lower panel illustrates the trend of mass-radius under the single-fluid scenario as a function of DM Fermi momentum by a wide space from 0.030 to 0.040 GeV. The Fermi momentum significantly affects both the maximum mass and radius of a NS, with both mass and radius decreasing significantly as the Fermi momentum increases. It can be observed that the Fermi momentum near 0.337 MeV can effectively meet the massive NS observation as well as the constraints from HESS J1713 − 347. For comparison, we also present the case of a NS obtained from pure baryon matter within the GM1 set, depicted by a black dashed line in the figure. Clearly, the radius of pure baryon matter is difficult to reconcile

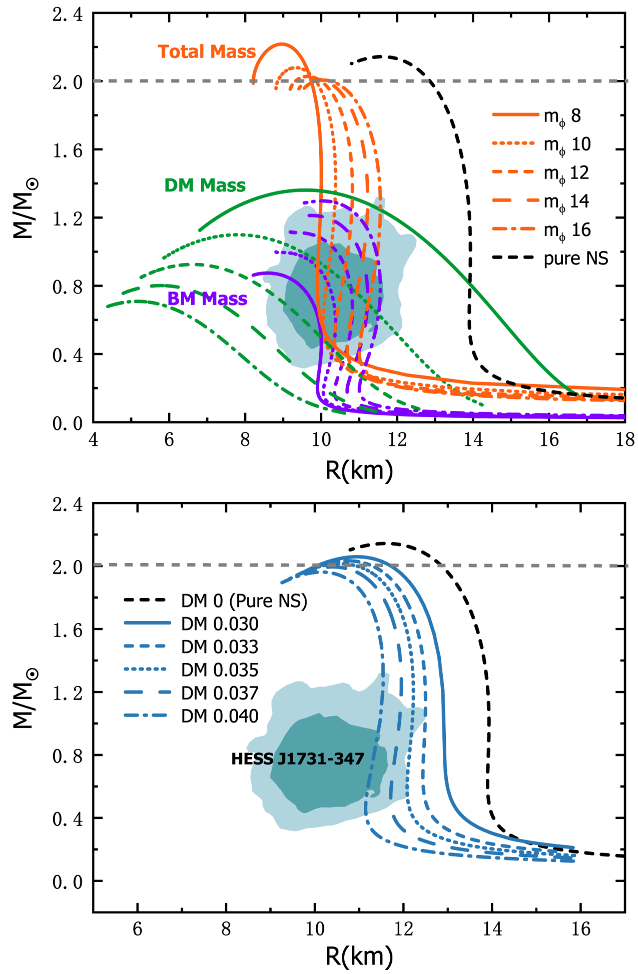

FIG. 1. Under the GM1 parameter set, the mass-radius relationships for two classes of DM models, with the shaded region representing the mass-radius confidence interval for compact star in HESS J1731 − 347. Upper panel (two-fluid DM model): the light green curve represents the mass-radius relationship for DM, while the purple curve represents that for BM. The orange curve depicts the total gravitational mass-radius relationship (with mass as the sum of DM and BM, and BM radius regarded as the observable radius). Different curves of the same color indicate different mediator mass. Lower panel (single-fluid DM model): the mass-radius relationships corresponding to different DM Fermi momentum. For comparison, the black dashed line in both models represents the NS mass-radius relationship for pure nucleonic matter under the GM1 parameter set.

TABLE II. In light of current multimessenger observational constraints, including $2M_\odot$ observations, as well as GW170817, PSR J0740 + 6620, PSR J0030 + 0451, and Rotation J1748 − 2446ad, in addition to the GM1 set, we further constrain the possible values of mediator mass in the two-fluid model and DM Fermi momentum in single-fluid model by other three different sets of relativistic parameter: BigApple [15], FSUGold [68], and IU-FSU [69].

CASES	m_ϕ (MeV)	k_F (GeV)
GM1	$10.0 \sim 15.0$	$0.033 \sim 0.038$
BigApple	$10.5 \sim 17.0$	$0.030 \sim 0.039$
FSUGold	$9.0 \sim 14.0$	$0.035 \sim 0.036$
IU-FSU	$11.0 \sim 16.0$	$0.032 \sim 0.037$

with the HESS J1713 − 347. It is worth noting that in Fig. 1 we only conducted a simple investigation of the advantage of two DM types in characterizing the HESS J1713 − 347, and in order to provide more comprehensive results in accordance with constraints impose by multimessenger observations, we offer a more detailed discussion in Fig. 5 and Table II.

In contrast to the single-fluid model, where the BM and DM components are uniformly mixed, in the case of the two-fluid model, the distributions of DM and BM often differ. When the DM radius R_D is greater than that of the BM component R_B, DM envelops BM, forming a dark matter halo. Conversely, when R_D is less than R_B, BM envelops DM, forming a dark matter core. In this paper, we will analyze three scenarios for the DM distribution: (a) fixed DM fraction $f_{\rm DM}$ with varying m_ϕ, (b) fixed m_ϕ with varying $f_{\rm DM}$, and (c) equal central pressure for DM and BM.

For the first two scenarios (a) and (b), we select the most typical $1.4M_\odot$ DM-mixed neutron star for discussion. In Fig. 2, the relationships between respective component central pressure and their radii are depicted for mediator mass m_ϕ ranging from 8 to 16 MeV, with the DM fraction $f_{\rm DM}$ fixed at 50%. Solving the TOV equations for two-fluid components reveals that when each component reaches its boundary, the pressure rapidly approaches zero, marking the corresponding component radius shown by solid black line (BM component) and dashed red line (DM component). It can be observed that when m_ϕ is 8 MeV the DM radius R_D is greater than R_B, leading to the formation of a DM halo. At this point, the central pressure of DM component is lower than that of BM. As m_ϕ increases, the radius of the DM component decreases, resulting in a more compact core, accompanied by a gradual increase in central pressure. Around 12 MeV, the DM halo begins to transition toward a DM core, and at $m_\phi = 16$ MeV, R_B becomes greater than R_D, forming a DM core. In Fig. 3, the DM distribution is shown for $m_\phi = 12$ MeV, with DM fractions of 50%, 30%, and 10%. As the DM fraction decreases, the DM central pressure continuously decreases, accompanied by a gradual increase in its R_D. Therefore, a lower mediator mass m_ϕ or a lower DM fraction makes it easier to form a DM halo.

Currently, the DM capture in NSs remains somewhat unclear, and theoretical discussions primarily focus on scenarios a and b, where the pressures of DM and BM at NS cores are not equal. To address this scenario theoretically, we assume equal central pressures for the BM and DM components and determine the corresponding component radii through the two-fluid TOV equations. Figure 4(a) illustrates the radii of the DM and BM components as a function of central pressure for different m_ϕ. The black line and red line represent the corresponding radius for the BM and DM components. The black squares indicate points where R_B equals R_D for different m_ϕ, which

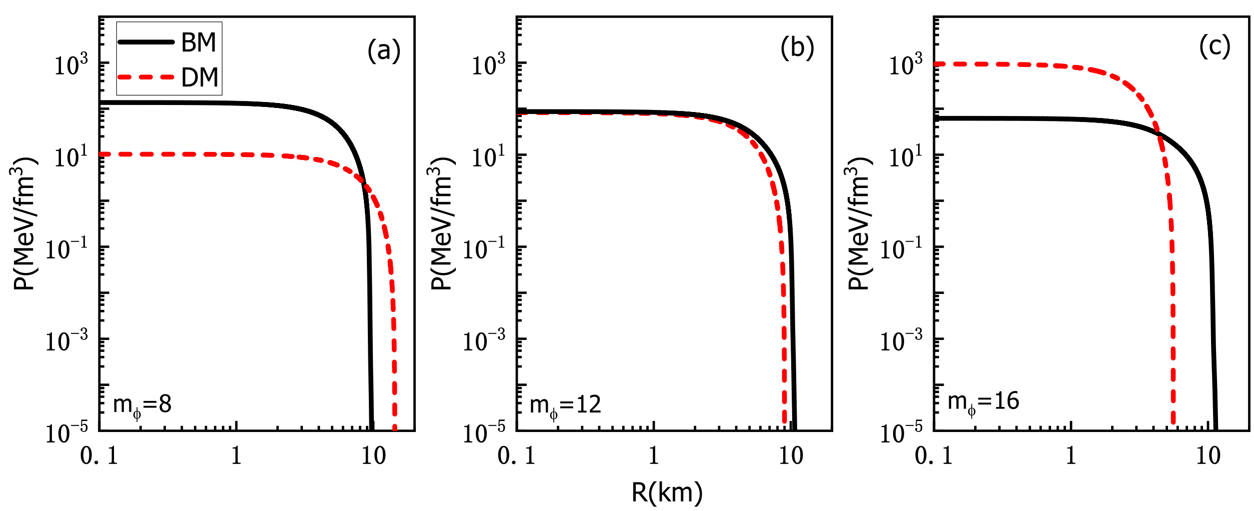

FIG. 2. In the scenario where dark matter fraction of 50%, the variation of central pressure with radius within a $1.4M_\odot$ DM-mixed NS for different mediator masses (a) 8 MeV, (b) 12 MeV, and (c) 16 MeV. The solid black line and the dashed red line represent BM and DM components, respectively. An increase in the mediator mass leads to the transition of DM halo toward DM core.

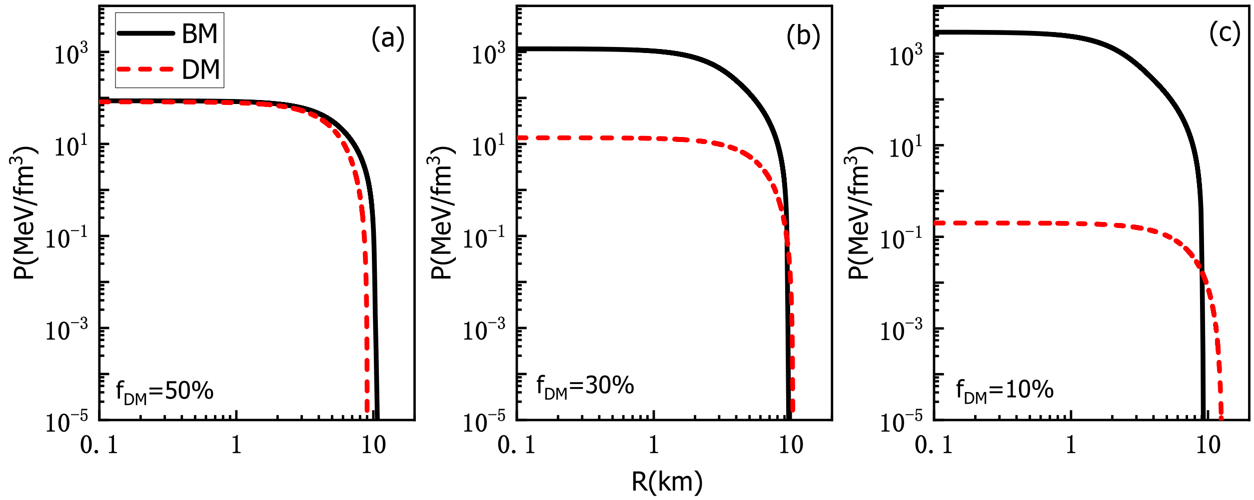

FIG. 3. In the scenario with mediator mass of 12 MeV, the variation of central pressure as a function of radius within a $1.4M_\odot$ DM-mixed NS for different DM fractions (a) 50%, (b) 30%, and (c) 10%. The solid black line and dashed red line represent BM and DM components, respectively. A decrease in the DM fraction leads to the transition of the DM core into the DM halo.

are the central pressure points for the two components. The black arrows indicate that above this central pressure R_D is smaller than R_B, resulting in the formation of a DM core, while the red arrows indicate that below this central pressure R_D is greater than R_B, leading to the formation of a DM halo. Additionally, for m_ϕ ranging from 12 to 16 MeV, under the same central pressure, R_D remains consistently smaller than R_B, indicating the formation of only a DM core. Figure 4(b) displays the DM fraction under different central pressures. As m_ϕ increases, the DM fraction decreases. Furthermore, for a given m_ϕ, when the central pressure values for both the DM and BM components exceed 200 MeV/fm^3, the DM fraction no longer varies with pressure. Based on the results presented in Fig. 1, it can be observed that satisfying both the requirements for the observation of massive NSs and the constraints imposed by HESS J1713 − 347 is challenging for both two-fluid and single-fluid models. To provide a more precise determination of the parameter ranges for these two models, extensive numerical calculations was conducted. Given the DM parameter ranges presented in Fig. 1, we divided the Fermi momentum range in the single-fluid

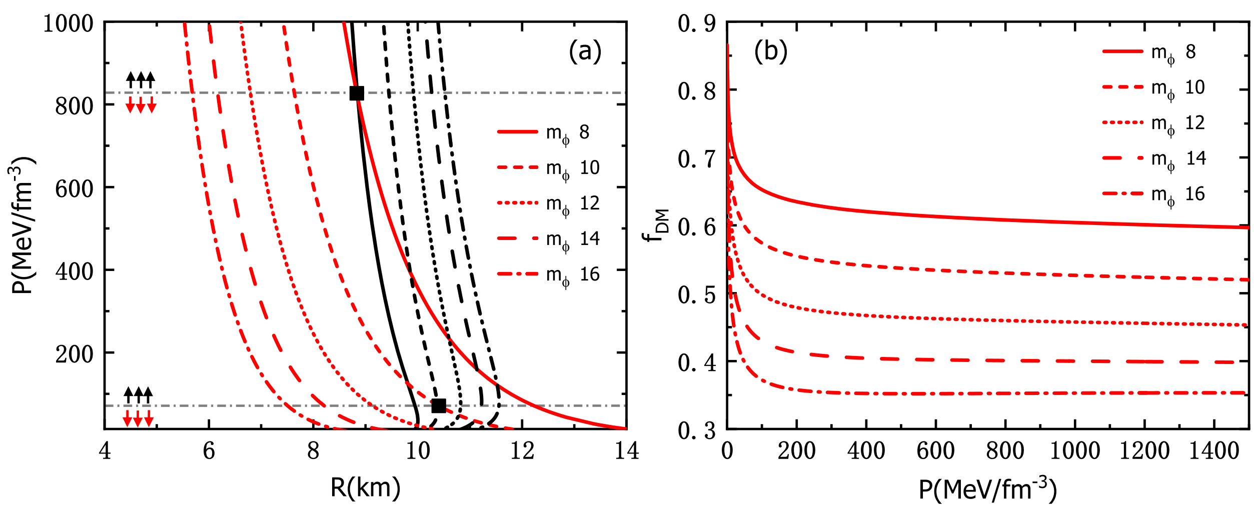

FIG. 4. (a) The relationship between central pressure and their respective component radii (red for DM and black for BM) under various mediator mass m_ϕ (different curves) for two-fluid model. Square intersections indicate points where the radius of DM component equals the radius of BM component for a specific m_ϕ. The region above the intersections shows that the BM radius is greater than the DM radius (black arrows), indicating the formation of a DM core above this central pressure, while the region below the intersections (red arrows) suggests the formation of a DM halo. (b) The variation of the DM fraction with central pressure under different m_ϕ.

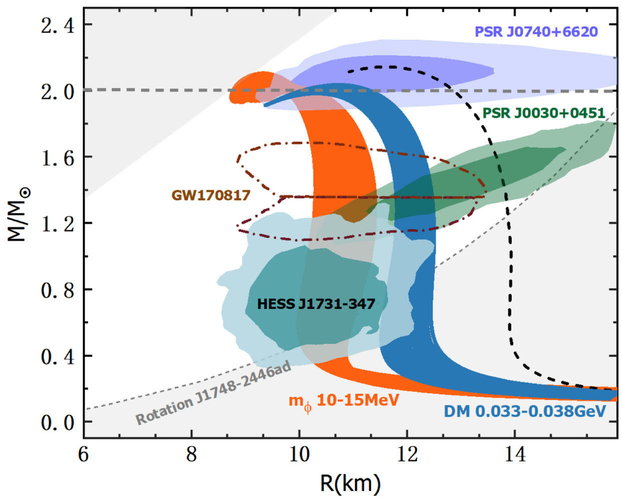

FIG. 5. Parameter space exploration under astronomical observational constraints for two DM models within GM1 set. The brown dashed line indicates the observation constraints from GW170817. The shaded regions represent the mass-radius constraints for three NSs: PSR J0740 + 6620, PSR J0030 + 0451, and HESS J1731 − 347. The gray regions in the top-left corners correspond to the causality and the bottom-right corners correspond to the forbidden region imposed by the fastest spin radio pulsar NS J1748 − 2446ad. The range of mediator mass values ($10 \sim 15$ MeV) satisfying all astronomical constraint requirements for the two-fluid models is shown in orange, while the range of Fermi momentum values ($0.033 \sim 0.038$ GeV) is indicated in dark blue. The black dashed line represents the mass-radius relationship for pure nucleonic matter in NSs.

model and the mediator mass range in the two-fluid model at equal intervals. Here, we discretized their respective ranges into 100 groups, and for each of these 100 groups, we input the corresponding EOS into the TOV equation to calculate the mass-radius relationship for these two DM models. Within the results, only the parameter range satisfying the constraints imposed by multimessenger astrophysical observations are retained, as depicted in Fig. 5 with the orange and dark blue regions corresponding to the two-fluid and single-fluid models, respectively. In the two-fluid model that meets all observational requirements, the mediator mass should be within the range of 10–15 MeV, and values lower than this range will violate causality (as indicated by the gray region in the upper-left corner), while values higher than this range cannot support recent $2M_\odot$ NS observation. For the single-fluid DM model, it requires the Fermi momentum to be within the range of 0.033–0.038 GeV, as values below this range cannot meet the observational constraints of HESS J1713 − 347 [18], and values above this range cannot support the observation of $2M_\odot$. In addition to satisfying the aforementioned observations, the parameter ranges for both models also comply with the observational constraints of GW170817 [10,11], PSR J0740 + 6620 [8,9], and PSR J0030 + 0451 [12,13]. Along with these, we also incorporate the constraint from the radio pulsar NS J1748 − 2446ad, the fastest-spin known pulsar located in the globular cluster Terzan having a spin frequency $f = \Omega/(2\pi) \approx 716$ Hz with Ω being angular velocity, reported in 2006 by Hessels et al. [88]. This can be used to help us further constrain the associated EOS [89], as depicted in the bottom right corner of Fig. 5, representing the forbidden region imposed by the NS J1748 − 2446ad. It is worth noting that these conclusions were also tested under different parameter sets, including the FSUGold, BigApple, and IU-FSU sets. The results, as shown in Table II, reveal relatively small differences, with all of them centered around a mediator mass of approximately 12 MeV and a Fermi momentum of approximately 0.035 GeV. Although this conclusion still exhibits some parameter dependence, it is evident from the results that both single-fluid and two-fluid models considering DM mixed can effectively meet astronomical observational constraints, especially including HESS J1731 − 347.

To further investigate the specific impact of these two different DM models on NS-related gravitational wave properties, such as tidal deformability, nonradial oscillation frequencies, and gravitational wave during the binary NS inspiral phase, we focus on the GM1 parameter set for both models in the subsequent discussion. For the single-fluid model, three different Fermi momentum values within the range defined in Table II (0.033, 0.035, and 0.037 GeV) are considered. For the two-fluid model, three different mediator mass are explored, namely, 10, 12, and 14 MeV. Their corresponding EOS are illustrated in Fig. 6. It should be noted that the single-fluid model yields a stiffer EOS compared to the two-fluid model, resulting in larger mass for the same radius, as reflected in Fig. 5.

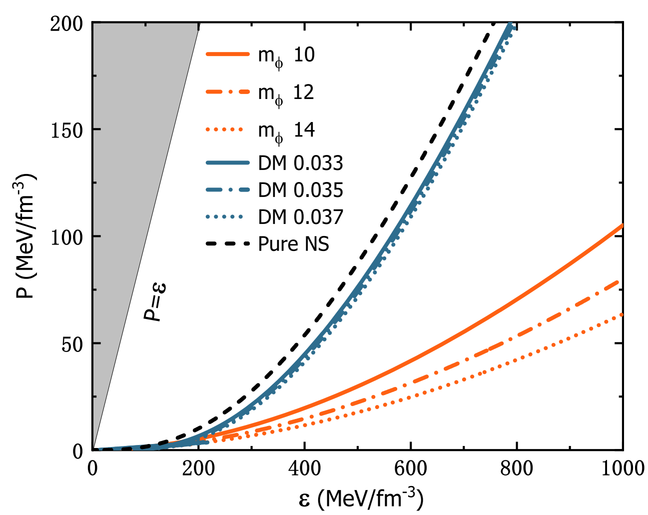

FIG. 6. Equation of states curves for two DM models, where orange represents the two-fluid model, dark blue represents the single-fluid model, and the black dashed line represents the pure NS.

III. NUMERICAL RESULTS ON NS GRAVITATIONAL WAVE

A. NS tidal deformability

Tidal deformability is an extractable parameter characterizing the NS distortion subjected to the tidal field of its companion star, and it serves as a crucial astronomical observable for NS EOS [90–93]. Dimensionless tidal deformability is defined as $\Lambda = \frac{2}{3}k_2/C^5$, where C is the compact parameter represented by M/R, a key physical quantity governing the tidal deformability value and also affecting gravitational wave signals during the binary NS merger process [94]. The parameter k_2, also known as the Love number, typically falls in the range of 0.05 to 0.15 for NSs and is highly dependent on the stellar structure [92,93]. The analytical expression can be expressed by the formula [90]

$$\begin{aligned} k_2 = {} & \frac{8C^5}{5}(1-2C)^2[2+2C(y_R-1)-y_R] \\ & \times \{2C(6-3y_R+3C(5y_R-8)) \\ & + 4C^3[13-11y_R+C(3y_R-2)+2C^2(1+y_R)] \\ & + 3(1-2C)^2[2-y_R+2C(y_R-1)]\log(1-2C)\}^{-1}; \end{aligned} \tag{40}$$

here, the physical quantity y_R satisfies the following differential equation

$$r\frac{dy_R(r)}{dr} + y_R(r)^2 + y_R(r)F(r) + r^2Q(r) = 0. \tag{41}$$

The energy density and pressure involved in the expressions for $F(r)$ and $Q(r)$ are different for single-fluid and two-fluid models. In the case of a single-fluid model, it is necessary to jointly determine k_2 by incorporating its corresponding single-fluid TOV equation [Eq. (28)]. There is a substantial body of literature available on this process, and we recommend Refs. [91–93]. For the two-fluid model, the process is similar, although its solution is slightly more complicated as it needs to consider the two-fluid forms of $F(r)$ and $Q(r)$ and also needs to simultaneously associate the two-fluid TOV equations [Eq. (30)] for a numerical solution. For a detailed discussion and derivation for this process, please see Ref. [95].

Figure 7(a) presents the relationships between dimensionless tidal deformability Λ and total DM-mixed NS gravitational mass for two DM models. As a comparison, the RMF parametrization of GM1 which for pure baryon matter (as shown by the black dashed line) is excluded by the gravitational wave measurement of GW170817 can be reconciled with tidal deformability measurement when considering DM mixed models for both single-fluid and two-fluid scenarios. Additionally, the tidal deformability values under the two-fluid model are smaller than those under the single-fluid model, implying that NSs under the two-fluid model are less prone to distort in its companion star tidal field than those under the single-fluid model.

Moreover, the differences between the two models are more pronounced in the low-mass region. At $1.4M_\odot$, the tidal deformability under the two-fluid model is approximately 150, while the single-fluid model yields results around 500. Around $2M_\odot$, both models produce Λ near 10

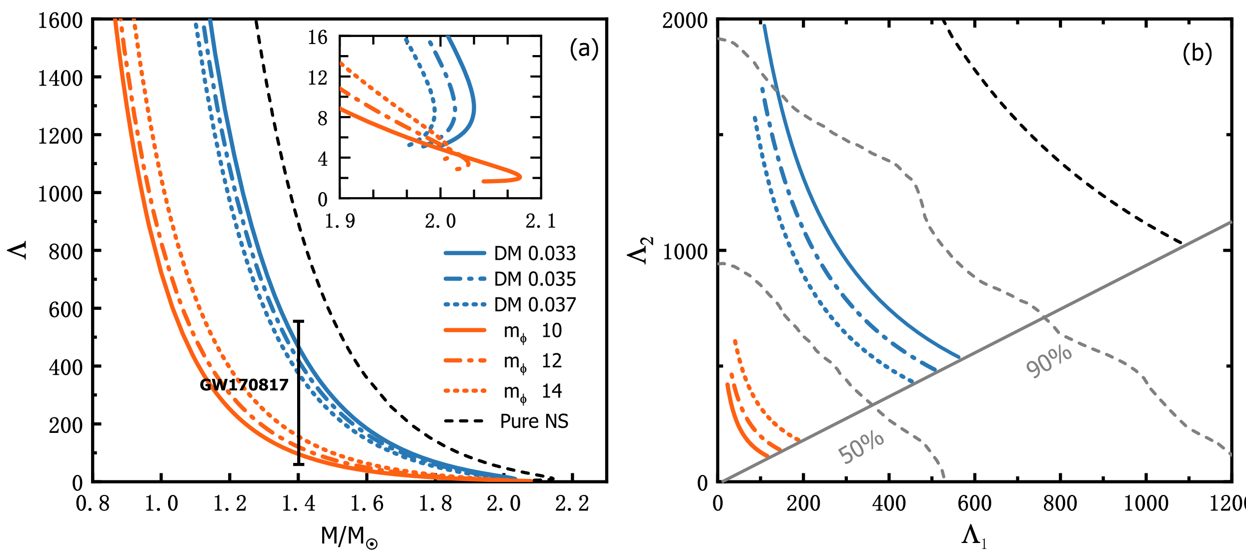

FIG. 7. (a) The tidal deformability of DM-mixed NS as a function of mass. Orange represents different DM mediator mass in the two-fluid model, dark blue represents different Fermi momenta for single-fluid model, and the black solid line represents the tidal deformability range extracted from the gravitational wave GW170817. (b) Relationship between tidal deformabilities Λ_1 and Λ_2 in the GW170817 event calculated under two different DM models, with gray dashed lines representing 50% and 90% credible intervals. The black dashed line represents the pure NS within the RMF parametrization of GM1, which is excluded by the GW170817 measurement.

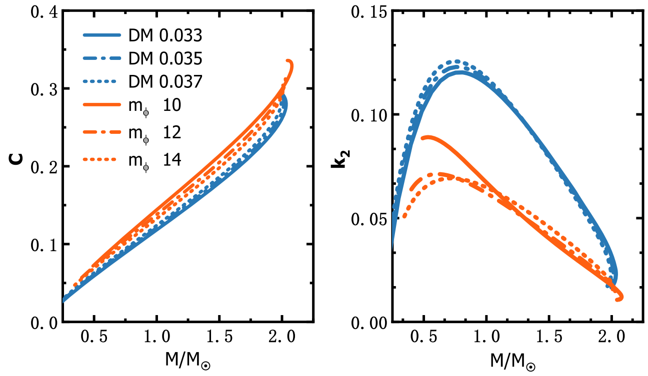

FIG. 8. Left panel: the relationship between compactness parameter C and NS mass in different DM models. Right panel: the relationship between tidal Love number k_2 and NS mass.

(as shown in the upper-right corner). Insights from Fig. 8 reveal that tidal deformability depends on the compactness parameter C and the Love number k_2. It can be observed that the differences in the compactness parameter C between the two models are minimal. However, there is a substantial difference in k_2 at $1.4M_\odot$, while the differences at $2M_\odot$ are less pronounced. Although the baryon component employs the same RMF model, tidal deformability is highly sensitive to the EOS. Since the results show that different DM models still have a considerable impact on its values, and would lead to noticeable tidal-related modifications in the gravitational wave emission during the inspiral phase (as discussed in Sec. III C).

Furthermore, in Fig. 7(b), we also calculate the individual tidal deformability for two NSs in the GW170817 event. We consider the most credible chirp mass with $[(m_1 m_2)^{3/5}]/[(m_1 + m_2)^{1/5}] = 1.188M_\odot$ [96], where m_1 and m_2 represent the high-mass and low-mass NSs, respectively. The gray dashed lines indicate the 50% and 90% credible intervals. Both classes of DM models fall within the credible interval range, while leaving the pure NS models outside.

B. Nonradial oscillation in DM-mixed NSs

As is well known, any nonaxisymmetric perturbation within a NS interior could generate gravitational waves. These perturbations can be classified into different oscillation modes, such as the f mode, gravitational g mode, pressure p mode, and rotational r mode, depending on the specific restoring forces involved [97–99]. These distinct modes are highly dependent on the internal structure and composition of a NS. Among these modes, the nonradial f mode is the most likely to produce gravitational radiation and is expected to be detected by the third-generation observatories like Cosmic Explorer and Einstein Telescope [41–43], offering a novel perspective on deciphering the NS internal structure.

In this study, we employed the Cowling approximation method under both single-fluid and two-fluid models. This approach neglects space-time metric perturbations but retains density perturbations [100–102]. Extensive research has shown that, in comparison to employing the complete linearized general relativity, the Cowling approximation method introduces a deviation of approximately 20% when calculating f-mode properties and only a 10% discrepancy for p modes [103], while the error for g modes is even lower [104].

In the context of two different DM models, we have computed the most typical quadrupole oscillations ($l = 2$), as illustrated in Fig. 9(a). The nonradial oscillation frequency of the f mode as a function of DM-mixed NS mass exhibits a striking similarity between these two DM models, and at around $1.4M_\odot$, the f-mode frequencies for both models are approximately around 2 kHz, while at $2M_\odot$, they are roughly situated near 2.7 kHz. However, distinguishing between these two DM models solely based on the f-mode frequencies appears to be a challenging task due to their values being very close to each other, and even these theoretical values hold promising prospects for detection by third-generation gravitational wave detectors.

Gravitational wave asteroseismology also enables us to establish a connection between the oscillation frequencies and its timescales with NS bulk properties [105–110]. For instance, the f-mode frequencies directly depend on the star average density, as initially proposed by Andersson and Kokkotas [111,112]. By incorporating realistic EOS, they established this relationship as

$$f(\mathrm{kHz}) = a + b\sqrt{\frac{\bar{M}}{\bar{R}^3}}, \tag{42}$$

where $\bar{M}/\bar{R}^3$ stands for the average density with $\bar{M}$ being dimensionless mass ($\bar{M} = M/1.4M_\odot$) and $\bar{R}$ being the dimensionless radius ($\bar{R} = R/10$ km). Another similar universal relation is an excellent linear correlation between ωM and M/R with $\omega M = a(M/R) - b$ and has been used to analyze the g mode, p mode, and f mode.

Figures 9(b) and 9(c), respectively, depict the fitting relationships corresponding to these two DM models. In the case of single-fluid one, strong linear correlations are observed for both types of universal relations at different DM Fermi momentum. Specifically, the fitting for the f-mode frequency with average density is found to be $f_0 = 1.7277\sqrt{\bar{M}/\bar{R}^3} + 0.86633$, while the fitting for ωM with the compact parameter C yields $\omega M = 208.1434(M/R) - 6.6903$. These results differ noticeably from previous studies for pure NSs [105]. Furthermore, in the two-fluid model, the linear fitting results for both the f mode and ωM differ. This discrepancy arises from the assumption that within the two-fluid model the DM-mixed NS gravitational mass is the sum of DM and BM components in both DM halo and DM core scenarios, while the DM-mixed NS radius always adopts the BM radius.

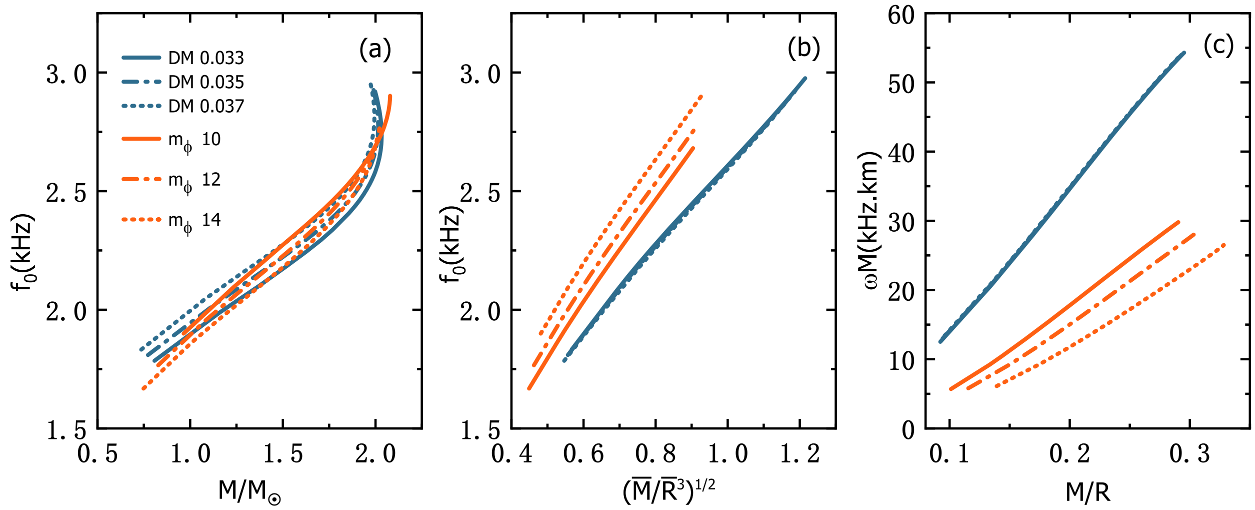

FIG. 9. (a) Nonradial oscillation frequency versus DM-mixed NS mass for different DM models. (b) Relationship between the nonradial oscillation of different DM models with the NS effective density. (c) Relationship between ωM and M/R for different DM models.

Overall, NSs with mixed DM components exhibit different linear relationships compared to those composed solely of BM. This distinction can serve as an indicator to assess whether DM components are within NSs, and moreover, there are also noticeable differences between various DM models.

C. Binary NS inspiral gravitational wave in quasicircular orbits

The EOS for NSs plays a pivotal role not only in determining bulk properties such as mass, radius, the moment of inertia, and gravitational redshift but also leaves a profound imprint on the gravitational waveforms associated with binary NS system [113]. Recent observations of binary NS mergers and NS-black hole mergers have been tirelessly peeling away the layers of uncertainty surrounding the NS internal composition, making it imperative to theoretically understand the EOS [38,39]. The binary NS merger process is typically divided into three phases: inspiral, merger, and ringdown [113]. The inspiral phase can be effectively modeled using the post-Newtonian (PN) approximation [114–117], which is an expansion of general relativity assuming low-velocity and weak-field conditions, and its validity has been firmly established [118,119]. In the PN approximation, the inspiral phase treats the binary system as a quasiperiodic orbit, necessitating the calculation of motion equations and correction terms in the gravitational wave signal to high orders, i.e., expanded in powers of $v/c \sim (GM/rc^2)^{1/2}$, where $(1/c)^n$ terms in the expansion represent the $\frac{n}{2}$PN expansion [114,115].

In this section, to compare the gravitational waves of binary NS within different DM models, we adopt the Taylor-T4 expanded PN method [115]. This approach is theoretically well suited for characterizing the gravitational waves emitted during the inspiral phase of dense binary star mergers. In the quasistationary phase of binary radiation, the system luminosity ($\mathcal{L}$) should be in balance with the time-dependent decay of energy (E),

$$\mathcal{L} = -\frac{dE}{dt} = -\frac{dE/dx}{dt/dx}, \tag{43}$$

where $x = (M_{\mathrm{tot}}\frac{d\Phi}{dt})^{2/3} = (M_{\mathrm{tot}}\Omega)^{2/3}$ is a gauge-independent PN parameter. Here, M_{tot} represents the total mass of the binary star system, Φ denotes the orbital phase, and Ω characterizes the orbital angular velocity. For a binary star system with a total mass of $M_{\mathrm{tot}} = M_1 + M_2$ spiraling in a circular orbit with angular velocity Ω, its gravitational energy is approximated at the 3.5PN order as [114,120,121]

$$E = -\frac{M_{\mathrm{tot}}\eta x}{2}\left\{1 + \left(-\frac{3}{4} - \frac{\eta}{12}\right)x + \left(-\frac{27}{8} + \frac{19\eta}{8} - \frac{\eta^2}{24}\right)x^2 + \left[-\frac{675}{64} + \left(\frac{34445}{576} - \frac{205\pi^2}{96}\right)\eta - \frac{155\eta^2}{96} - \frac{35\eta^3}{5184}\right]x^3\right\}, \tag{44}$$

where $\eta = m_1 m_2/M_{\mathrm{tot}}^2$ represents the symmetric mass ratio for binary NSs. At distances far from the source, gravitational perturbations are linear, and the luminosity can be expressed in the following form [121]:

$$\mathcal{L} = \frac{r^2}{32\pi}\int d\Omega \langle \dot{h}_{ij}^{\mathrm{TT}} \dot{h}_{ij}^{\mathrm{TT}} \rangle. \tag{45}$$

Under the 3.5PN order approximation, the luminosity $\mathcal{L}$ is expressed as [115,121,122]

$$\mathcal{L} = \frac{32\eta^2 x^5}{5}\left\{1 + \left(-\frac{1247}{336} - \frac{35\eta}{12}\right)x + 4\pi x^{3/2} + \left[\frac{6643739519}{69854400} + \frac{16\pi^2}{3} - \frac{1712\gamma_E}{105} - \frac{856}{105}\ln(16x)\right.\right.$$
$$\left. + \left(-\frac{134543}{7776} + \frac{41\pi^2}{48}\right)\eta - \frac{94403\eta^2}{3024} - \frac{775\eta^3}{324}\right]x^3 + \left(-\frac{16285}{504} + \frac{214745\eta}{1728} + \frac{193385\eta^2}{3024}\right)\pi x^{7/2}$$
$$\left. + \left(-\frac{44711}{9072} + \frac{9271\eta}{504} + \frac{65\eta^2}{18}\right)x^2 + \left(-\frac{8191}{672} - \frac{583\eta}{24}\right)\pi x^{5/2}\right\}, \tag{46}$$

where $\gamma_E \approx 0.5772$ is the Euler-Mascheroni constant. The dominant ($l = 2, m = 2$) modes of the gravitational waveform can be decomposed into spin-weighted spherical harmonics [123–125]

$$h_{22} = -8\sqrt{\frac{\pi}{5}}\frac{M_{\mathrm{tot}}\eta}{D}e^{-2i\phi}x\left\{1 + \left(-\frac{107}{42} + \frac{55\eta}{42}\right)x + \left[\frac{27027409}{646800} - \frac{856\gamma_E}{105} + \frac{2\pi^2}{3} + \frac{428i\pi}{105} - \frac{428}{105}\ln(16x)\right.\right.$$
$$\left. + \left(\frac{41\pi^2}{96} - \frac{278185}{33264}\right)\eta - \frac{20261\eta^2}{2772} + \frac{114635\eta^3}{99792}\right]x^3 + \left(-\frac{2173}{1512} - \frac{1069\eta}{216} + \frac{2047\eta^2}{1512}\right)x^2 + 2\pi x^{3/2}$$
$$\left. + \left[-\frac{107\pi}{21} + \left(\frac{34\pi}{21} - 24i\right)\eta\right]x^{5/2}\right\}, \tag{47}$$

where D represents the distance between the source and the observer, and in our calculations, we adopt a typical value of 100 Mpc. The orbital phase Φ of the binary star system can be obtained through the following integral equation:

$$\frac{dx}{dt} = -\frac{\mathcal{L}}{dE/dx}, \tag{48}$$

$$\frac{d\phi}{dt} = \frac{x^{3/2}}{M}. \tag{49}$$

The solution to this integral equation is typically achieved using the TaylorT1-TaylorT4 method, and in this paper, we employ the TaylorT4 method. Furthermore, during the binary star inspiral process, tidal interactions have a significant impact on the dynamics. Therefore, it is necessary to additionally account for the effects from tidal interactions in the formulas [126–128]

$$\frac{\mathrm{d}x}{\mathrm{d}t} = \frac{64\eta}{5M_{\mathrm{tot}}}x^5\{F^{\mathrm{T4}}_{3.5}(x) + F^{\mathrm{T4}}_{\mathrm{Tidal}}(x)\}, \tag{50}$$

where $F^{\mathrm{T4}}_{3.5}(x)$ is the PN expansion expression given under the TaylorT4 method,

$$F^{\mathrm{T4}}_{3.5}(x) = 1 - \left(\frac{743}{336} + \frac{11}{4}\eta\right)x + 4\pi x^{3/2} + \left(\frac{34103}{18144} + \frac{13661}{2016}\eta + \frac{59}{18}\eta^2\right)x^2 - \left(\frac{4159}{672} + \frac{189}{8}\eta\right)\pi x^{5/2}$$
$$+ \left[\frac{16447322263}{139708800} - \frac{1712}{105}\gamma_E - \frac{56198689}{217728}\eta + \frac{541}{896}\eta^2 - \frac{5605}{2592}\eta^3 + \frac{\pi^2}{48}(256 + 451\eta)\right.$$
$$\left. - \frac{856}{105}\ln(16x)\right]x^3 + \left(-\frac{4415}{4032} + \frac{358675}{6048}\eta + \frac{91495}{1512}\eta^2\right)\pi x^{7/2}. \tag{51}$$

The tidal correction term $F^{\mathrm{T4}}_{\mathrm{Tidal}}(x)$ accurate to 1PN, as provided by Vines [94], is given by

$$F^{\mathrm{T4}}_{\mathrm{Tidal}}(x) = \frac{32\chi_1\lambda_2}{5M^6_{\mathrm{tot}}}\left[12(1 + 11\chi_1)x^{10} + \left(\frac{4421}{28} - \frac{12263}{28}\chi_2 + \frac{1893}{2}\chi_2^2 - 661\chi_2^3\right)x^{11}\right] + (1 \leftrightarrow 2),$$

where x_1 and x_2 represent the binary NS mass ratios and λ_1 and λ_2 denote the respective tidal deformability values. For equal-mass binary NS systems, the $F^{\mathrm{T4}}_{\mathrm{Tidal}}(x)$ can be expressed in the form [127]

$$F^{\mathrm{T4}}_{\mathrm{Tidal}}(x) = \frac{52}{5M_{\mathrm{tot}}}\frac{k_2}{C^5}x^{10}\left(1 + \frac{5203}{4368}x\right), \tag{52}$$

in which C and k_2 characterize the compactness parameter and tidal Love number, respectively. Although tidal interactions only come into play at the fifth post-Newtonian (5PN) order during the binary NS inspiral phase, their

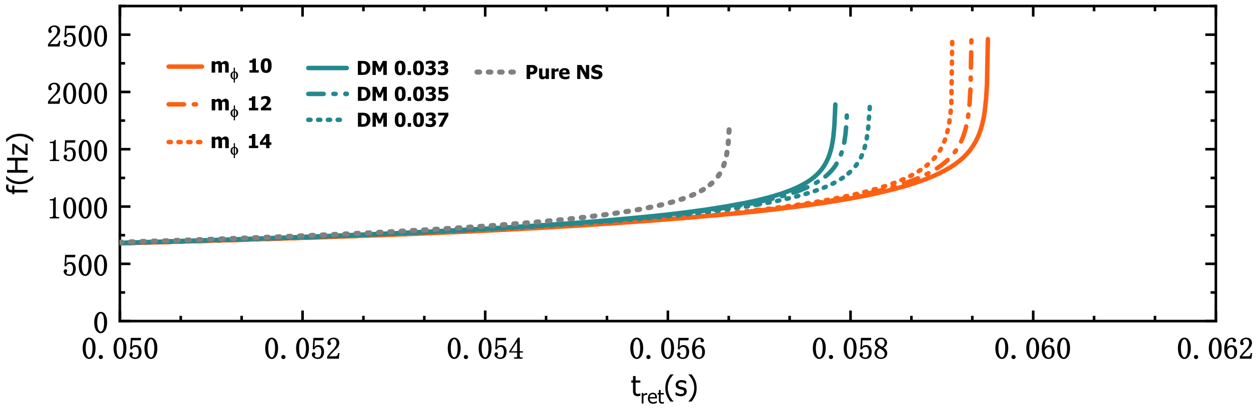

FIG. 10. The relationship between the gravitational wave frequency during the inspiral phase and the retarded time t_{ret} for different DM scenarios. The gray dashed line represents the frequency for the pure NS.

coefficients can reach magnitudes of 10^4, making tidal interactions play a crucial role. In this section, we consider the gravitational wave frequency and amplitude properties of a typical $1.35M_{\odot}$ binary NS in the inspiral phase, corresponding to a total system mass of $M_{\mathrm{tot}} = 2.7M_{\odot}$. The initial values in the integral equation are taken at the minimum gravitational wave frequency, $f = 371$ Hz, corresponding to $M_{\mathrm{tot}}\Omega_0 = 0.0155$. Observers calculate the source using the retarded time t_{ret}, defined as $t_{\mathrm{ret}} = t - r_*$, with r_* being the tortoise coordinate characterized by [127]

$$r_* = r_A + 2M_{\mathrm{tot}} \ln\left(\frac{r_A}{2M_{\mathrm{tot}}} - 1\right), \tag{53}$$

where $r_{\mathrm{A}} = \sqrt{A/4\pi}$ and A represents the proper sphere surface area. Figure 10 illustrates the variation of frequency with respect to inspiral time for different DM models. In comparison to the pure NS with an inspiral time of 0.0566s, DM-mixed NSs can sustain the inspiral phase for a longer duration. Furthermore, the two-fluid DM model exhibits a longer inspiral time than the single-fluid one, with an extension of approximately 2 ms. In the single-fluid scenario, the duration of the binary NS inspiral process is significantly influenced by the DM Fermi momentum, with a longer duration observed as k_F increases. For instance, a Fermi momentum of $k_F = 0.033$ GeV corresponds to a retarded time of 0.0578 s, while $k_F = 0.037$ GeV yields a retarded time of 0.0582 s. This trend arises because a higher DM component has a more pronounced impact on the mass-radius relationship. Figure 1(b) reveals that for larger DM Fermi momentum NSs with the same mass have smaller radii, making it more challenging for the occurrence of quadrupolar tidal deformability [as shown in Fig. 7(a)]. Consequently, the impact of tidal deformability during the binary NS inspiral process is less significant, resulting in a longer duration time. In the case of two-fluid models, a smaller mediator mass leads to a longer inspiral time. With $m_\phi = 10$ MeV, the retarded time is 0.0595 s, while $m_\phi = 14$ MeV results in a retarded time of 0.0591 s. This outcome mirrors the behavior observed in single-fluid models and is attributed to the same principle: a lower m_ϕ leads to smaller NS radius [as indicated in Fig. 1(a)] and make tidal interaction less likely to occur [see Fig. 7(a)], hence prolonging the inspiral duration. As for the frequency that increases as the binary NS system evolves, various models also exhibit obvious differences. Figure 10 shows that in the final inspiral stage the binary stars in the two-fluid model exhibit a shorter rotation period, resulting in higher gravitational wave frequencies, approximately around 2400 Hz. Following that is the frequency provided by the single-fluid model, with the lowest frequency being given by the pure NS model. It can be seen that the use of features from the inspiral duration time and gravitational wave frequency can clearly illustrate the discrepancy, further verifying the significant role played by DM in gravitational wave observations. To highlight the distinctions between these two DM models and compare them with pure NSs, we have compiled the retarded times and frequencies in Table III.

Figure 11 illustrates the strain amplitude of the (2,2) dominant mode with respect to the retarded time during the inspiral process of the $1.35M_{\odot}$ binary NS system. The upper panel shows waveforms for the two-fluid DM model, with solid colored lines representing different mediator

TABLE III. The frequencies and retarded times in binary NS inspiral phase for three different NS models.

CASES		Frequency (Hz)	t_{ret}(s)
Pure NS		1715.925	0.0566
Single-fluid model	$k_F = 0.033$	1891.079	0.0578
	$k_F = 0.035$	1887.756	0.0579
	$k_F = 0.037$	1900.486	0.0582
Two-fluid model	$m_\phi = 10$	2462.231	0.0595
	$m_\phi = 12$	2493.946	0.0593
	$m_\phi = 14$	2473.811	0.0591

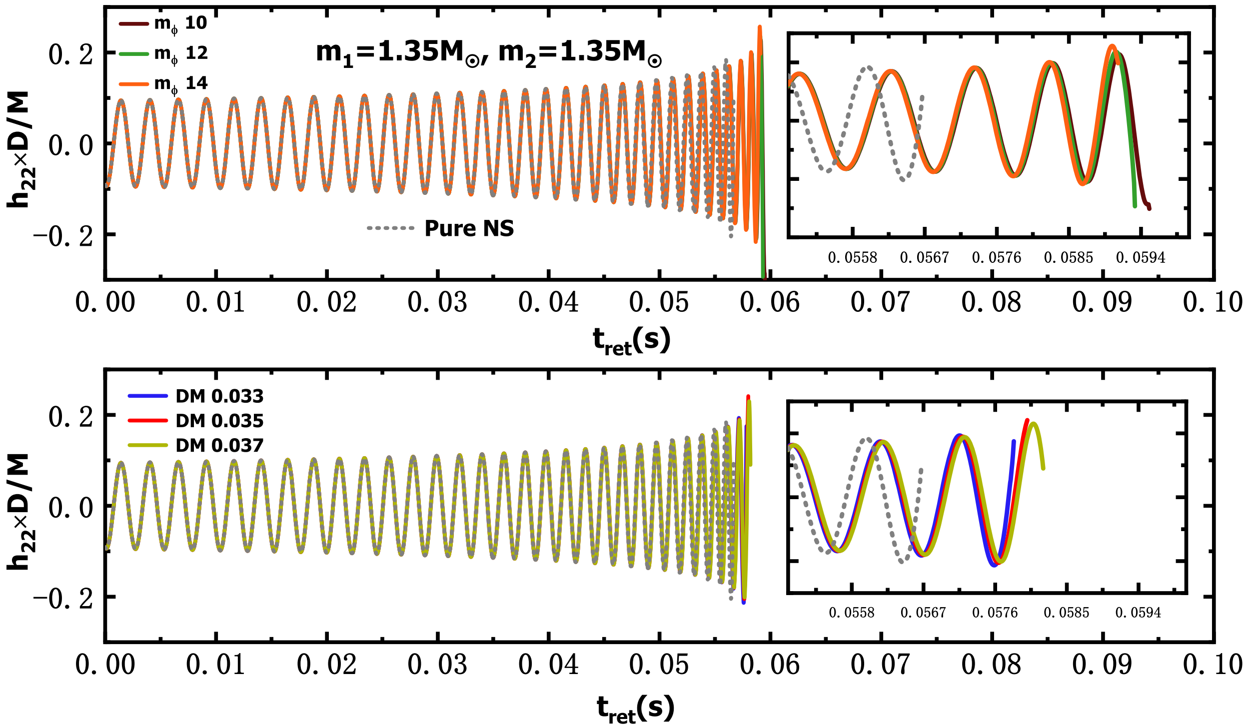

FIG. 11. Upper panel: in the two-fluid DM model, the relationship between the gravitational wave amplitude h_{22} and $t_{\rm ret}$ during the inspiral phase of $1.35M_\odot$ binary NSs. Lower panel: in the single-fluid DM model, the relationship between the gravitational wave amplitude h_{22} and $t_{\rm ret}$ during the inspiral phase of $1.35M_\odot$ binary NSs. The gray dashed line represents the waveform for the pure NS.

masses. The gravitational wave strain amplitude and frequency (see Fig. 10) increase continuously throughout the inspiral phase, reaching their maximum values in the final stages. Remarkably, the impact of different mediator masses on the gravitational waveforms and amplitudes is marginal, affecting primarily the duration of inspiral phase, as shown in the upper-right corner. Specifically, smaller mediator masses result in longer-lasting inspiral phases. The lower panel presents results for a single-fluid model, with colored solid lines denoting various Fermi momenta. Analogous to the two-fluid model, the impact on the waveforms and amplitudes remains modest, also predominantly affecting the inspiral duration, as demonstrated in the bottom-right corner, and a higher Fermi momentum k_F for DM results in a longer duration. Nevertheless, based on the gravitational waveforms and amplitude from Figs. 10 and 11, it remains challenging to separate these two different DM types. Within the sensitivity range of future-advanced gravitational wave detectors, there is promising to identify and constrain the DM models from the frequency and duration of inspiral phase. In contrast to the scenario of pure NSs, as shown by the gray dash line in both panels, significant differences in waveforms, frequencies, and inspiral times are evident, especially in the final stages. Although this study is limited to the GM1 parameter, we still have similar conclusions for the FSUGold [68], BigApple [15], and IU-FSU sets [69]. As a consequence, the DM plays a substantial role in the dynamical processes during the binary NS inspiral phase, underscoring the imperative need to incorporate DM effects. This not only facilitates an explanation for potentially missed gravitational wave emissions during the inspiral phase but also aids in achieving more stringent constraints on DM models.

IV. SUMMARY

In this study, we introduce DM components within NSs to construct DM-mixed NS models with two distinct DM types. One type employs a single-fluid approach, wherein DM interacts not only gravitationally with baryon components but also through nongravitational interactions involving Higgs boson exchange. Another type employs a two-fluid approach, where DM interacts with baryon component solely through gravitational interactions. In both DM scenarios, the interactions among baryon matter are described using the RMF theory. For the baryon model, we adopt the GM1 parameter, as it can provide solutions that well meet the constraints including the current $2M_\odot$ massive observation as well as the observation imposed by NICER on the PSR J0740 + 6620 and PSR J0030 + 0451. Our research reveals that the introduction of DM-admixed NS model within GM1 not only well satisfies the current various astronomical observations, including the $2M_\odot$ observation, PSR J0740 + 6620, PSR J0030 + 0451, GW170817, and Rotation J1748 − 2446ad, but more importantly also provides successful explanations for the small mass and radius observations of the central compact object in the supernova remnant HESS J1731 − 347.

In the two-fluid model, we explore three scenarios for DM distribution, (a) a fixed DM fraction f_{DM} with varying m_ϕ, (b) a fixed m_ϕ with varying f_{DM}, (c) identical central pressures for DM and BM components, and investigate their potential formation of dark matter cores and halos. It is found that in all three scenarios smaller mediator masses and lower DM fractions in DM-mixed NSs tend to favor the formation of DM halo structures. Furthermore, to avoid giving an overly absolute conclusion that the mixed-DM inside NSs can better meet the astronomical observations under only GM1 parameter in the paper, we actually considered three other relativistic parameter sets of FSUGold, BigApple, and IU-FSU. By incorporating current observations, we further narrow down the parameter space values for two DM models, yielding a mediator mass m_ϕ in the range of $10 \sim 15$ MeV and a DM Fermi momentum k_F in the range of $0.033 \sim 0.038$ GeV for GM1. Employing the same computational procedure as GM1, we obtain the ranges in m_ϕ ($9 \sim 14$ MeV) and k_F ($0.035 \sim 0.036$ GeV) for FSUGold, m_ϕ ($10.5 \sim 17$ MeV) and k_F ($0.030 \sim 0.039$ GeV) for BigApple, and m_ϕ ($11 \sim 16$ MeV) and k_F ($0.032 \sim 0.037$ GeV) for IU-FSU.

We also investigate the differences in gravitational wave related properties between the two models. In terms of tidal deformability, the RMF parametrization of GM1, which for baryon matter is excluded by the gravitational wave measurement of GW170817, can be reconciled with tidal deformability measurement when considering DM mixed models. Additionally, the tidal deformability values under the two-fluid model are smaller than those under the single-fluid model, implying that NSs under the two-fluid model are less prone to distort in its companion star tidal field than those under the single-fluid model. Regarding nonradial oscillations for DM-mixed NSs within GM1, the f-mode frequencies obtained from both DM models are remarkably close; however, they exhibit significant differences in universal relations. As for the gravitational wave generation during NS inspiral phase, the presence of DM, in comparison to a pure NS scenario within GM1, leads to a prolonged inspiral duration and higher gravitational wave frequency. Additionally, two-fluid models exhibit longer spindown timescales compared to single-fluid models. The mediator mass and Fermi momentum have minimal effects on the gravitational waveforms and amplitude throughout the entire inspiral phase but primarily influence its duration.

The above studies show that, although the search for DM and the determination of its components are still unclear, in any case, in a compact star such as a NS, in addition to the microscopic many-body theory between particles, the strong gravity will also make the internal coupling of DM possible, and therefore the reasonable introduction of DM components is beneficial. This allows for a better explanation of current observational phenomena to some extent and may be able to provide theoretical explanations for future high-sensitivity detectors to shed light on the possibilities of incorporating DM.

ACKNOWLEDGMENTS

The authors would like to express sincere gratitude to the anonymous reviewer for their valuable suggestions and comments on this paper. The authors also thank professor Jun Xu for his useful discussion. This work is supported by the National Natural Science Foundation of China (Grants No. 12035011 and No. 11975167), the National Key R&D Program of China (Contracts No. 2018YFA0404403), and the China Postdoctoral Science Foundation (Grant No. 2023M742668).

[1] M. Oertel, M. Hempel, T. Klähn, and S. Typel, Rev. Mod. Phys. **89**, 015007 (2017).
[2] G. Burgio, H.-J. Schulze, I. Vidaña, and J.-B. Wei, Prog. Part. Nucl. Phys. **120**, 103879 (2021).
[3] F. Özel and P. Freire, Annu. Rev. Astron. Astrophys. **54**, 401 (2016).
[4] P. B. Demorest, T. Pennucci, S. M. Ransom, M. S. E. Roberts, and J. W. T. Hessels, Nature (London) **467**, 1081 (2010).
[5] E. Fonseca, T. T. Pennucci, J. A. Ellis *et al.*, Astrophys. J. **832**, 167 (2016).
[6] Z. Arzoumanian, A. Brazier, S. Burke-Spolaor *et al.*, Astrophys. J. Suppl. Ser. **235**, 37 (2018).
[7] J. Antoniadis, P. C. C. Freire, N. Wex *et al.*, Science **340** 448 (2013).
[8] H. T. Cromartie, E. Fonseca, S. M. Ransom *et al.*, Nat. Astron. **4**, 72 (2020).
[9] E. Fonseca, H. T. Cromartie, and T. T. Pennucci, Astrophys. J. Lett. **915**, L12 (2021).
[10] B. P. Abbott, R. Abbott, T. D. Abbott *et al.* (LIGO Scientific and Virgo Collaborations), Phys. Rev. X **9**, 011001 (2019).
[11] M. Fasano, T. Abdelsalhin, A. Maselli, and V. Ferrari, Phys. Rev. Lett. **123**, 141101 (2019).
[12] M. C. Miller, F. K. Lamb, A. J. Dittmann, S. Bogdanov, Z. Arzoumanian *et al.*, Astrophys. J. **887**, L24 (2019).

[13] T. E. Riley, A. L. Watts, S. Bogdanov, P. S. Ray, R. M. Ludlam *et al.*, Astrophys. J. **887**, L21 (2019).
[14] A. Sedrakian, F. Weber, and J. J. Li, Phys. Rev. D **102**, 041301 (2020).
[15] F. J. Fattoyev, C. J. Horowitz, J. Piekarewicz, and B. Reed, Phys. Rev. C **102**, 065805 (2020).
[16] I. Bombaci, A. Drago, D. Logoteta, G. Pagliara, and I. Vidaña, Phys. Rev. Lett. **126**, 162702 (2021).
[17] F. Li, B.-J. Cai, Y. Zhou, W.-Z. Jiang, and L.-W. Chen, Astrophys. J. **929**, 183 (2022).
[18] V. Doroshenko, V. Suleimanov, G. Pühlhofer, and A. Santangelo, Nat. Astron. **6**, 1444 (2022).
[19] K. Huang, J. Hu, Y. Zhang, and H. Shen, Astrophys. J. **904**, 39 (2020).
[20] Y. Suwa, T. Yoshida, M. Shibata, H. Umeda, and K. Takahashi, Mon. Not. R. Astron. Soc. **481**, 3305 (2018).
[21] L. Brodie and A. Haber, Phys. Rev. C **108**, 025806 (2023).
[22] P. T. Oikonomou and C. C. Moustakidis, Phys. Rev. D **108**, 063010 (2023).
[23] J. J. Li and A. Sedrakian, Phys. Lett. B **844**, 138062 (2023).
[24] J. E. Horvath, L. S. Rocha, L. M. de Sá, P. H. R. S. Moraes, L. G. Barão, M. G. B. de Avellar, A. Bernardo, and R. R. A. Bachega, Astron. Astrophys. **672**, L11 (2023).
[25] S. Kubis, W. Wójcik, D. A. Castillo, and N. Zabari, Phys. Rev. C **108**, 045803 (2023).
[26] A. Quddus, G. Panotopoulos, B. Kumar, S. Ahmad, and S. K. Patra, J. Phys. G **47**, 095202 (2020).
[27] O. Lourenço, T. Frederico, and M. Dutra, Phys. Rev. D **105**, 023008 (2022).
[28] H. C. Das, A. Kumar, B. Kumar, S. K. Biswal, T. Nakatsukasa, A. Li, and S. K. Patra, Mon. Not. R. Astron. Soc. **495**, 4893 (2020).
[29] G. Bertone and D. Hooper, Rev. Mod. Phys. **90**, 045002 (2018).
[30] M. A. Buen-Abad, R. Essig, D. McKeen, and Y.-M. Zhong, Phys. Rep. **961**, 1 (2022).
[31] M. Haslbauer, P. Kroupa, A. H. Zonoozi, and H. Haghi, Astrophys. J. Lett. **939**, L31 (2022).
[32] T. Bessho, Y. Ikeda, and W. Yin, Phys. Rev. D **106**, 095025 (2022).
[33] S. Chatterjee, R. Garani, R. K. Jain, B. Kanodia, M. S. N. Kumar, and S. K. Vempati, Phys. Rev. D **108**, L021301 (2023).
[34] A. Tan *et al.* (PandaX-II Collaboration), Phys. Rev. Lett. **117**, 121303 (2016).
[35] C. Kouvaris and P. Tinyakov, Phys. Rev. D **83**, 083512 (2011).
[36] N. F. Bell, G. Busoni, T. F. Motta, S. Robles, A. W. Thomas, and M. Virgato, Phys. Rev. Lett. **127**, 111803 (2021).
[37] J. Coffey, D. McKeen, D. E. Morrissey, and N. Raj, Phys. Rev. D **106**, 115019 (2022).
[38] J. A. Faber and F. A. Rasio, Living Rev. Relativity **15**, 8 (2012).
[39] D. Radice, S. Bernuzzi, and A. Perego, Annu. Rev. Nucl. Part. Sci. **70**, 95 (2020).
[40] C. Aerts, Rev. Mod. Phys. **93**, 015001 (2021).
[41] S. E. Perkins, N. Yunes, and E. Berti, Phys. Rev. D **103**, 044024 (2021).
[42] M. Punturo, M. Abernathy, F. Acernese *et al.*, Classical Quantum Gravity **27**, 084007 (2010).
[43] S. Dwyer, D. Sigg, S. W. Ballmer, L. Barsotti, N. Mavalvala, and M. Evans, Phys. Rev. D **91**, 082001 (2015).
[44] J. Walecka, Ann. Phys. (N.Y.) **83**, 491 (1974).
[45] B. D. Serot, Rep. Prog. Phys. **55**, 1855 (1992).
[46] P. Ring, Prog. Part. Nucl. Phys. **37**, 193 (1996).
[47] G. F. Burgio, M. Baldo, P. K. Sahu, and H.-J. Schulze, Phys. Rev. C **66**, 025802 (2002).
[48] W.-C. Chen and J. Piekarewicz, Phys. Rev. C **90**, 044305 (2014).
[49] L. Tolos, M. Centelles, and A. Ramos, Astrophys. J. **834**, 3 (2016).
[50] S. K. Biswal, S. K. Patra, and S.-G. Zhou, Astrophys. J. **885**, 25 (2019).
[51] X. H. Wu and H. Shen, Phys. Rev. C **99**, 065802 (2019).
[52] O. Lourenço, M. Dutra, C. H. Lenzi, C. V. Flores, and D. P. Menezes, Phys. Rev. C **99**, 045202 (2019).
[53] B. Hong, Z. Ren, C. Wu, and X. Mu, Classical Quantum Gravity **40**, 125007 (2023).
[54] M. Baldo and G. Burgio, Prog. Part. Nucl. Phys. **91**, 203 (2016).
[55] B.-A. Li and X. Han, Phys. Lett. B **727**, 276 (2013).
[56] N. Paar, C. C. Moustakidis, T. Marketin, D. Vretenar, and G. A. Lalazissis, Phys. Rev. C **90**, 011304 (2014).
[57] K. Hebeler, J. M. Lattimer, C. J. Pethick, and A. Schwenk, Astrophys. J. **773**, 11 (2013).
[58] X. Roca-Maza, X. Viñas, M. Centelles, B. K. Agrawal, G. Colò, N. Paar, J. Piekarewicz, and D. Vretenar, Phys. Rev. C **92**, 064304 (2015).
[59] I. Tews, J. M. Lattimer, A. Ohnishi, and E. E. Kolomeitsev, Astrophys. J. **848**, 105 (2017).
[60] D. Adhikari, H. Albataineh, D. Androic *et al.* (PREX Collaboration), Phys. Rev. Lett. **126**, 172502 (2021).
[61] D. Adhikari, H. Albataineh, D. Androic *et al.* (CREX Collaboration), Phys. Rev. Lett. **129**, 042501 (2022).
[62] N. K. Glendenning and S. A. Moszkowski, Phys. Rev. Lett. **67**, 2414 (1991).
[63] V. B. Thapa and M. Sinha, Phys. Rev. C **105**, 015802 (2022).
[64] M. G. Alford, L. Brodie, A. Haber, and I. Tews, Phys. Rev. C **106**, 055804 (2022).
[65] D. Sen, N. Alam, and G. Chaudhuri, Phys. Rev. D **106**, 083008 (2022).
[66] L. L. Lopes, Commun. Theor. Phys. **74**, 015302 (2021).
[67] A. Kunjipurayil, T. Zhao, B. Kumar, B. K. Agrawal, and M. Prakash, Phys. Rev. D **106**, 063005 (2022).
[68] B. G. Todd-Rutel and J. Piekarewicz, Phys. Rev. Lett. **95**, 122501 (2005).
[69] F. J. Fattoyev, C. J. Horowitz, J. Piekarewicz, and G. Shen, Phys. Rev. C **82**, 055803 (2010).
[70] H. C. Das, A. Kumar, S. K. Biswal, and S. K. Patra, Phys. Rev. D **104**, 123006 (2021).
[71] G. Panotopoulos and I. Lopes, Phys. Rev. D **96**, 083004 (2017).
[72] B. Murakami and J. D. Wells, Phys. Rev. D **64**, 015001 (2001).

[73] Y. Meng *et al.* (PandaX-4T Collaboration), Phys. Rev. Lett. **127**, 261802 (2021).
[74] J. Oppenheimer and G. Volkoff, Phys. Rev. **55**, 374 (1939).
[75] G. Baym, C. Pethick, and P. Sutherland, Astrophys. J. **170**, 299 (1971).
[76] C. Gonzalez-Boquera, M. Centelles, X. Viñas, and L. M. Robledo, Phys. Lett. B **779**, 195 (2018).
[77] J. Carriere, C. J. Horowitz, and J. Piekarewicz, Astrophys. J. **593**, 463 (2003).
[78] J. Xu, L.-W. Chen, B.-A. Li, and H.-R. Ma, Astrophys. J. **697**, 1549 (2009).
[79] S. Kubis, Phys. Rev. C **70**, 065804 (2004).
[80] C. Gonzalez-Boquera, M. Centelles, X. Viñas, and T. R. Routray, Phys. Rev. C **100**, 015806 (2019).
[81] Q.-F. Xiang, W.-Z. Jiang, D.-R. Zhang, and R.-Y. Yang, Phys. Rev. C **89**, 025803 (2014).
[82] O. Ivanytskyi, V. Sagun, and I. Lopes, Phys. Rev. D **102**, 063028 (2020).
[83] C. Kouvaris and N. G. Nielsen, Phys. Rev. D **92**, 063526 (2015).
[84] M. Pospelov and A. Ritz, Phys. Rev. D **84**, 113001 (2011).
[85] B. Bhattacherjee, S. Matsumoto, S. Mukhopadhyay, and M. M. Nojiri, J. High Energy Phys. 10 (2013) 032.
[86] A. Maselli, P. Pnigouras, N. G. Nielsen, C. Kouvaris, and K. D. Kokkotas, Phys. Rev. D **96**, 023005 (2017).
[87] S. L. Shapiro and S. A. Teukolsky, *Black Holes, White Dwarfs, and Neutron Stars: The Physics of Compact Objects* (John Wiley & Sons, New York, 1983).
[88] J. W. T. Hessels, S. M. Ransom, I. H. Stairs, P. C. C. Freire, V. M. Kaspi, and F. Camilo, Science **311**, 1901 (2006).
[89] V. Sagun, E. Giangrandi, T. Dietrich, O. Ivanytskyi, R. Negreiros, and C. Providência, Astrophys. J. **958**, 49 (2023).
[90] T. Hinderer, Astrophys. J. **677**, 1216 (2008).
[91] T. Hinderer, B. D. Lackey, R. N. Lang, and J. S. Read, Phys. Rev. D **81**, 123016 (2010).
[92] J. Hu, S. Bao, Y. Zhang, K. Nakazato, K. Sumiyoshi, and H. Shen, Prog. Theor. Exp. Phys. **2020** (2020).
[93] T. Malik, N. Alam, M. Fortin, C. Providência, B. K. Agrawal, T. K. Jha, B. Kumar, and S. K. Patra, Phys. Rev. C **98**, 035804 (2018).
[94] J. Vines, E. E. Flanagan, and T. Hinderer, Phys. Rev. D **83**, 084051 (2011).
[95] A. Das, T. Malik, and A. C. Nayak, Phys. Rev. D **105**, 123034 (2022).
[96] B. P. Abbott, R. Abbott, T. D. Abbott *et al.* (LIGO Scientific and Virgo Collaborations), Phys. Rev. Lett. **119**, 161101 (2017).
[97] K. D. Kokkotas and B. F. Schutz, Mon. Not. R. Astron. Soc. **255**, 119 (1992).
[98] H. K. Lau, P. T. Leung, and L. M. Lin, Astrophys. J. **714**, 1234 (2010).
[99] K. D. Kokkotas and B. G. Schmidt, Living Rev. Relativity **2**, 2 (1999).
[100] T. G. Cowling, Mon. Not. R. Astron. Soc. **101**, 367 (1941).
[101] P. N. McDermott, H. M. van Horn, and J. F. Scholl, Astrophys. J. **268**, 837 (1983).
[102] A. Torres-Forné, P. Cerdá-Durán, A. Passamonti, and J. A. Font, Mon. Not. R. Astron. Soc. **474**, 5272 (2017).
[103] S. Yoshida and Y. Kojima, Mon. Not. R. Astron. Soc. **289**, 117 (1997).
[104] H. Sotani, K. Tominaga, and K.-i. Maeda, Phys. Rev. D **65**, 024010 (2001).
[105] D. D. Doneva, E. Gaertig, K. D. Kokkotas, and C. Krüger, Phys. Rev. D **88**, 044052 (2013).
[106] O. Benhar, V. Ferrari, and L. Gualtieri, Phys. Rev. D **70**, 124015 (2004).
[107] A. Passamonti, E. Gaertig, K. D. Kokkotas, and D. Doneva, Phys. Rev. D **87**, 084010 (2013).
[108] E. Gaertig, K. Glampedakis, K. D. Kokkotas, and B. Zink, Phys. Rev. Lett. **107**, 101102 (2011).
[109] B. K. Pradhan and D. Chatterjee, Phys. Rev. C **103**, 035810 (2021).
[110] D.-H. Wen, B.-A. Li, H.-Y. Chen, and N.-B. Zhang, Phys. Rev. C **99**, 045806 (2019).
[111] N. Andersson and K. D. Kokkotas, Phys. Rev. Lett. **77**, 4134 (1996).
[112] N. Andersson and K. D. Kokkotas, Mon. Not. R. Astron. Soc. **299**, 1059 (1998).
[113] E. Burns, Living Rev. Relativity **23**, 4 (2020).
[114] L. Blanchet, Living Rev. Relativity **9**, 4 (2006).
[115] M. Boyle, D. A. Brown, L. E. Kidder, A. H. Mroué, H. P. Pfeiffer, M. A. Scheel, G. B. Cook, and S. A. Teukolsky, Phys. Rev. D **76**, 124038 (2007).
[116] H. C. Das, A. Kumar, and S. K. Patra, Mon. Not. R. Astron. Soc. **507**, 4053 (2021).
[117] A. Buonanno and B. S. Sathyaprakash, arXiv:1410.7832.
[118] L. Blanchet, G. Faye, and F. Larrouturou, Classical Quantum Gravity **39**, 195003 (2022).
[119] A. Chattaraj, T. RoyChowdhury, Divyajyoti, C. K. Mishra, and A. Gupta, Phys. Rev. D **106**, 124008 (2022).
[120] M. Maggiore, *Gravitational Waves: Volume 1: Theory and Experiments* (Oxford University Press, New York, 2007).
[121] B. D. Lackey, The neutron-star equation of state and gravitational waves from compact binaries, Ph.D. thesis, The University of Wisconsin-Milwaukee, 2012.
[122] L. Blanchet, B. R. Iyer, and B. Joguet, Phys. Rev. D **65**, 064005 (2002).
[123] L. E. Kidder, Phys. Rev. D **77**, 044016 (2008).
[124] Q. Henry, Phys. Rev. D **107**, 044057 (2023).
[125] G. Faye, S. Marsat, L. Blanchet, and B. R. Iyer, Classical Quantum Gravity **29**, 175004 (2012).
[126] A. Buonanno, B. R. Iyer, E. Ochsner, Y. Pan, and B. S. Sathyaprakash, Phys. Rev. D **80**, 084043 (2009).
[127] K. Hotokezaka, K. Kyutoku, and M. Shibata, Phys. Rev. D **87**, 044001 (2013).
[128] K. Hotokezaka, K. Kyutoku, Y.-i. Sekiguchi, and M. Shibata, Phys. Rev. D **93**, 064082 (2016).